EFFECTS OF VARIATIONS IN CONTROLLER GAINS ON THE DYNAMICS OF MAGNETIC BEARINGS

by

David R. Schmiel

Thesis submitted to the faculty of

Virginia Polytechnic Institute and State University

in partial fulfillment of the requirements for the degree of

MASTER OF SCIENCE

in

MECHANICAL ENGINEERING

Approved:

Prof. H. H. Cudney (Chair)

Prof. R.G. Kirk

Prof. H.H. Robertshaw

May 1996

key words: magnetic bearings, control systems, rotor dynamics, turbomachinery, dynamic properties

EFFECTS OF VARIATIONS IN CONTROLLER GAINS ON THE DYNAMICS OF MAGNETIC BEARINGS

by

David R. Schmiel

Prof. H.H. Cudney, Chair

Department of Mechanical Engineering

Virginia Polytechnic Institute and State University

(ABSTRACT)

Magnetic bearings support turbomachinery by regulating their forces exerted in relation to the displacement of the machine supported. The regulating control system must be tuned for stable and safe operation of the rotor. The ultimate goal of this study is to determine the effects of changing controller gains on the behavior of the rotor during operation in its normal speed range with a known unbalance load. We also endeavor to confirm the model of the rotor supported the magnetic bearings, as an additional goal.

We first investigate the modelling of rotors supported by magnetic bearings, including the model of the control system. We present a finite element model of a magnetic bearing supported rotor, and perform experiments to determine the characteristics of the control system which governs the magnetic forces on the rotor. The experimental control system characteristics confirm the expected characteristics from

theory. With this knowledge, we perform simulations and experiments under the same forcing conditions to determine the accuracy of the model in predicting the experimental behavior of an unbalanced rotor. The model exhibits satisfactory ability in predicting the experimental behavior of the rotor under this loading. Our next step is to determine the effects of variation of proportional and integral controller gains on the behavior of the rotor. Both simulations and experiments show that an increase in the proportional controller gain results in an increase in the rotor's first critical speed. An increase in the integral gain results in a small decrease in the location of the peak response speed in the speed range tested, while leaving the peak amplitude insignificantly changed. Again, simulations and experiments predict this result.

We reach the following three conclusions from this study. First, the finite element model of the rotor/bearing system is a viable model for predicting the behavior of the experimental system. Second, tuning of the proportional gain shows a significant effect on the behavior of the rotor during unbalance loading across its speed range, due to considerable change in bearing stiffness caused by the tuning of this gain. Last, tuning of the integral gain has a small effect on the behavior of the rotor due to the change in bearing damping, too small to be considered significant.

Acknowledgments

There are a lot of people that I need to thank here. However, I don't want to write another thesis of acknowledgments, so if you know me, and you don't see your name mentioned and you feel slighted, I apologize upfront. With that out of the way, let's get on with the show.

I would like to thank my advisor, Prof. Harley Cudney, for his advice, encouragement, and suggestions throughout my Masters' program, and indeed during my senior year when I worked for him as an undergraduate researcher. It has been a privilege to work with Prof. Cudney. I'd also like to thank Prof. Gordon Kirk for the use of his laboratory and for his expertise in the field of rotor dynamics. Finally, it's been a tremendously enjoyable experience knowing Prof. Harry Robertshaw. From Digital Control to "Hey, Schmiel's back in town!", I can always count on Harry to be interesting and funny.

Next, the guys (and one gal) in the lab deserve recognition. From when I first stepped into the Active Adaptive Structures and Control Systems Laboratory, I felt welcome and at ease. Thanks for your encouragement and friendship, everyone: Anton Sumali, Chris Niezrecki, Rich Lomenzo, Larry Tentor, Rodney Red Wing, Jon Hill, Ana Moyka, Tom McCray, and Wes Holley.

The other lab (the Rotor Dynamics Laboratory) also deserves recognition. Erik Swanson, especially, gave me invaluable assistance on the experimental portion of this work. Without his help, I never would have finished. Erik, I think the magnetic bearing

rig is safe now that my work is done. Krish Ramesh provided me with the models used in this thesis, and gave me invaluable information concerning rotor modeling. Finally, K.V.S. Raju and John Wang were always around to talk to and never failed to lift my spirits.

Outside of the labs, there are a lot of other people in and out of the department who offered friendship and support who deserve thanks: Chris Fannin, Andy Wright, Scott Houser, Mike DeLorenzo, Susan Larkin, Mike Scardina and Soo Kang, Randy and Anita Soper (and their new arrival!), and Lauren Lenchner. I'd also like to thank my employers at PDI for being patient with me while I finished my thesis.

Of course, all thanks are due to my family. My parents, Gene and Bonnie Schmiel, always provided me with love, encouragement, and support in the good times and the bad. My sister, Jennifer Schmiel, now an experienced college student herself, was always there with an encouraging word and an upbeat attitude. Thanks Mom, Dad, and Jenn, I love you all.

Finally, I would like to dedicate this thesis to my late maternal grandfather, Robert L. Elliott II. An engineer with TRW for 43 years, he represents a standard which I will be lucky to reach. Thanks for passing on the engineering genes, Grandpa.

Table of Contents

List of Figures

List of Tables

Nomenclature

c	damper value
c_{eff}	effective damping
g	acceleration due to gravity
$[i]$	vector of bearing currents
i_c	measured bearing current
i_o	coil current at which ball is suspended
j	square root of -1
k	stiffness value
k_{eff}	effective stiffness
k_x	force-position relationship
k_i	force-current relationship
$[k_i]$	matrix of bearing force-current values
$[k_z]$	matrix of magnetic bearing position stiffnesses
k_z	magnetic bearing position stiffness
m	mass in examples
$m\text{-}e$	mass-eccentricity value
s	laplace variable
x_o	position at which ball is suspended
x	ball position
x_n	rotor displacement in the x-direction at the nth mass station

y_n rotor displacement in the y-direction at the nth mass station

[z] rotor coordinate vector

A state space state dynamics matrix

A_g projected magnet area

B state space input matrix

C state space output matrix

$[C_{eff}]$ effective rotor damping matrix

$[C_{eq}]$ equivalent bearing damping matrix

[C] rotor damping matrix

D state space feedthrough matrix

F_{ext} external force

F_p control input to plant

$[F_{ext}]$ vector of external rotor forces

$[F_{mb}]$ vector of magnetic bearing forces

[G] rotor gyroscopic matrix

G(s) feedback control transfer function

$G_{aa}(s)$ anti-alias filter transfer function

$G_s(s)$ sensor gain

$G_{pad}(s)$ pre A/D filter transfer function

$G_{pda}(s)$ post D/A filter transfer function

$G_{pid}(s)$ transfer function of PID controller

G_{amp} amplifier gain

G nominal air gap

[G(s)] transfer function matrix relating current to position

I_b bias current in bearing

IG integral gain in S2M nomenclature

[I(s)] laplace transform of bearing current vector

[K] rotor stiffness matrix

$[K_{eq}]$ equivalent bearing stiffness matrix

$[K_{eff}]$ effective rotor stiffness matrix

K_d derivative controller gain

K_p proportional controller gain

K_i integral controller gain in theoretical examples

[M] rotor mass matrix

N number of coil turns per magnet pole pair

P_{loss} phase loss

P(s) plant transfer function

Q peak magnification factor

R_{net} net response

V_{in} measured DSP voltage input

V_{out} measured amplifier voltage output

[Z(s)] laplace transform of bearing position coordinate vector

δx position perturbation

ω_s rotor spin speed

Θ_{xn} rotor angular displacement in the x-direction at the nth mass station

Θ_{yn} rotor angular displacement in the y-direction at the nth mass station

ω rotor whirl frequency

μ_o permeability of free space

ω_n natural frequency

ζ damping ratio

Chapter 1: Introduction

1.1 Background

The use of magnetic bearings in the support of industrial turbomachinery has increased steadily over the past ten years. Magnetic bearings offer several advantages over conventional journal bearings such as tilting-pad or fluid film bearings. First, the non-contact characteristic of magnetic bearings results in longer life of both bearing and shaft. Second, the range of operating temperatures and environments is much wider because of the lack of need for lubricating fluids such as oils. Third, the dynamic properties of the bearings can be adjusted so that the designer can place peak rotor vibration levels at desired frequencies, or decrease rotor vibration levels at undesirable frequencies.

One disadvantage of magnetic bearings is that they are inherently unstable without active feedback control. For stable operation of the rotor, we need to tune the control system so that the rotor/bearing system is stable across the range of running speeds.

Industrial turbomachines such as compressors or turbines are usually designed to run in a range of design speeds. The bearings which support such machinery play a large role in the vibration characteristics of the machine, such as peak response amplitudes, peak response speeds, and ease of passage through a critical speed. The bearings must be chosen or designed so that vibration levels are not excessively high at or near running

speed. Also, if the running speed is higher than the first critical speed, passage through this critical speed should be smooth and not result in excessively large amplitudes.

1.2 Motivation

We are motivated to perform the research presented in this thesis because the need exists to understand how control system parameters affect rotor performance. With this knowledge, guidelines can be created for the design of control systems for magnetic bearings. This thesis will provide the necessary background to design new control systems for new magnetic bearing supported rotors.

1.3 Objective

Currently, at the Rotor Dynamics Laboratory, an industrial digital control cabinet donated by Societe de Mechanique Magnetic (S2M) of France controls the magnetic bearings supporting the 3-disk stainless steel rotor, one of several rotor test rigs at the laboratory. Ultimately, we would like to replace this control cabinet with a new digital control system, with which we would have complete tuning capability. As it stands now, the controller is limited by the program code donated by S2M.

We first intend to understand and verify the analytical model of the rotor supported by the magnetic bearings with the current control system. We will use this knowledge to predict the behavior of the rotor under the influence of the magnetic bearings. We will then determine how parameter variations in the controller affects the

stability and response of the rotor, and use the analytical model of the system as confirmation of the results of our experiments.

1.4 Approach

To accomplish our objectives, we take the following steps. We will develop a model for the rotor supported by magnetic bearings. We perform simulations to predict the response of the rotor to an unbalance excitation with the current control system in place. We will experimentally verify these predictions. We will then determine analytically how a discrete PID (Proportional-Integral-Derivative) control algorithm affects a magnetic bearing's damping and stiffness, and how these properties affect stability and response of the rotor/bearing system. Our next step is to make changes in the current control program settings, simulate the response with these changes, and confirm our simulation results with experiments. Finally, we will use the knowledge gained in the process of this research to recommend control strategies for a new magnetic bearing supported rotor.

1.5 Literature Review

The literature review has revealed that much work has been performed in the area of magnetic bearing control systems. In particular, researchers have focused their efforts on three aspects of magnetic bearings, control systems, and rotor dynamics: the modelling of rotor/magnetic bearing systems, the control of magnetic bearings using

several different types of control algorithms, and the control of magnetic bearings using the PID (Proportional-Integral-Derivative) compensator. This review will show the major contributions from these three areas, and the contribution of this thesis to the area researched will be outlined at the end of this review.

Several sources show the concept of magnetic suspension of a small object such as a steel ball. Franklin, Powell, and Emami-Naeini [5], demonstrated the need for feedback control to keep a steel ball suspended stably. They showed the suspension of a steel ball under electromagnetic forces, including a force model linearized about the suspension point. This example is important because it is totally analogous to the operation of magnetic bearings.

The modelling of rotor/bearing systems with magnetic bearings has received extensive treatment. The two main modelling techniques that the literature review revealed are: the finite element model, and the single degree of freedom model. The finite element model treats the rotor as a series of point masses interconnected by massless connectors. The advantage to this technique is that the large of number of resulting coordinates in the mathematical model results in accurate reflection of the true dynamics of the rotor. The main disadvantage is that computation time for simulation with a larger model is considerably longer than the single degree of freedom approach. The single degree of freedom approach has the advantage of simple analysis for low frequency ranges. However, higher order dynamics are not reflected in this modelling technique, rendering it inaccurate beyond the rigid modes of the rotor.

Barrett [2] demonstrated a finite element model of an magnetic bearing supported rotor which includes the effects of hydrodynamic seals and gyroscopic moments. He also partitioned the rotor model to separate the coordinates of interest (sensed and controlled coordinates) from the other coordinates and demonstrated several methods to solve for the stability and forced response of a magnetic bearing supported rotor, based on the control system's transfer function. Maslen and Bielk [10] derived a matrix model of a magnetic bearing supported rotor which augmented a standard state space formulation of the rotor with controller state variables to produce a single state space model containing both rotor and controller state variables. Their model includes effects of sensor-actuator noncolocation and a detailed model of the control system, including controller bandwidth. They demonstrated how to perform stability analysis with their augmented model to determine the stability of free vibrations of a controlled magnetic bearing supported rotor. Ramesh [13] demonstrated several different methods to model magnetic bearing supported turbomachinery. In particular, he demonstrated a method by which the control system's dynamic characteristics are calculated at frequencies of interest. These characteristics are inserted into the rotor model's stiffness and damping matrices for stability or forced response analysis at the desired frequency.

The different approaches to controlling magnetic bearings highlight a variety of control methods. The unifying factor in the different approaches is the goal of regulating the position of the rotor so as to minimize whirl amplitudes during operation. Humphris *et al.* [8] showed the effects of varying control system bandwidth on bearing properties,

as well as regions of stable operation for proportional and rate gain changes. They determined that a control system with higher bandwidth (50 KHz) results in a much wider stability range than a control system with lower bandwidth (1.2 KHz). They also developed a method to experimentally measure bearing properties and showed that bearing stiffness varied linearly with proportional controller gain, while bearing damping varied linearly with derivative controller gain. Finally, they experimentally determined an upper stability limit for bearing stiffness.

Chen and Darlow [3] utilized velocity and acceleration observers for rotating force control of magnetic bearings. The observers provided signals of rotor velocity and acceleration based on displacement measurements without performing any differentiation. The velocity signal was used to set the magnetic bearing damping while the acceleration signal created a rotating force which canceled external disturbances such as unbalance forces. They determined that the velocity observer was effective and is a better and inexpensive alternative to differentiation circuits. They also concluded that the acceleration observer is best suited for lightly damped critical speed vibration suppression.

Youcef-Toumi and Reddy [17] implemented a digital Time Delay Controller in a magnetic bearing system as an alternative to an existing linear analog compensator. They developed a model of the entire system including actuator dynamics, rigid and flexible rotor dynamics, and identified and validated models of various components of the system. The effectiveness of the Time Delay Controller was validated based upon computer

simulations and experiments. They showed that the Time Delay Controller has much better static and dynamic stiffness characteristics than their previous analog compensator. Finally, the Time Delay Controller maintained almost the same behavior over a wide range of rotor running speeds.

Salm [14] utilized a reduced order rotor model for controller design, and addressed the problem of control spillover into higher frequency rotor modes. He described a direct-output feedback control scheme which guarantees stability despite spillover if certain system requirements are fulfilled. With the control system experimentally implemented, the flexible rotor passed through five critical speeds with low vibration levels.

The classical PID (Proportional-Integral-Derivative) compensator has proven very popular and effective for the control of active magnetic bearings. Because the effective bearing properties of stiffness and damping can be easily determined from the PID gains, the effectiveness of gain combinations is more easily gauged, and the tuning process is simpler as well. Keith *et al* [9] designed and developed a digital control system for a magnetic bearing supporting rotor. Implementing a digital PD (Proportional-Derivative) algorithm on this digital control system yielded results similar to those with an analog PD controller. They showed for both controllers that changing proportional gain changed the magnetic bearing stiffness, while changing derivative gain changed the bearing damping. Experimentally, both controllers were effective at changing the bearing properties and allowed significant changes in the vibration amplitudes and critical speeds of the rotor.

Allaire, Humphris, and Barrett [1] showed the effects of proportional and rate (derivative) gains on the unbalance response of a magnetic bearing supported rotor. Experimentally, increasing the controller proportional gain by a factor of five more than doubled the rotor's first critical speed, while increasing the controller derivative gain by a factor of four decreased the peak amplitude at the first critical speed by a factor of five.

Williams, Keith, and Allaire [16] investigated the effects of digital proportional, integral, derivative, and second derivative control (PIDD) on the bearing properties. They showed that proportional gain affects the bearing stiffness, derivative gain affects the bearing damping, and integral gain affects damping at lower frequencies, while having an insignificant effect at higher frequencies. They experimentally demonstrated the effects of varying these controller parameters on the rotor response across the range of running speeds. They also investigated the effects of second-derivative control and digital sampling rate on the properties. They showed that the bearing stiffness is relatively unchanged by a variation in second-derivative gain, while the damping at high frequencies is changed significantly. They showed that increasing the sampling rate has the same effect as increasing the second derivative gain.

The contribution of this work, with respect to the previous work cited, is as follows. The previous work cites many experimental results which show the effects of controller parameter variation. Simulations are also mentioned frequently as a method of prediction of these experimental results, with reduced order single degree of freedom models. However, to our knowledge, no one has directly compared simulation data from

a finite element model to experiments which varied controller parameters. We do this as a method of comparison and validation of the experimental results with respect to the model of the system.

1.6 Thesis Overview

Chapter 2 of this work discusses the physical characteristics of the magnetic bearing test rig, including the physical dimensions of the rotor, disks, and bearings, and the electronic components of the control system. We discuss the basic operation of magnetic bearings, and the finite element modelling of a rotor. We show a simple magnetic suspension system's open loop instability, make the analogy between this system and magnetic bearings, and conclude that we require a control system for rotor position regulation. We also review the components of the feedback control loop which produces the magnetic bearing force based on rotor position. Chapter 3 reiterates the need for feedback control to stabilize the system, shows effective properties of a general control system, and how these properties affect a simple mechanical system's properties. The effective damping and stiffness of varying Proportional-Integral-Derivative controller gains are shown in graphical form, and we show their implementation into a rotor/bearing model. We then review the program provided by S2M to tune the control system and show the effective properties of the control system with the current system settings. Finally, we show a design example for a magnetic

suspension device and make the analogy between the design procedure shown and control system design for magnetic bearings.

Chapter 4 discusses the analytical and experimental work performed. We show experiments to identify the characteristics of several portions of the control loop. We show experiments to verify the model of the controlled rotor, and view the changes in forced response characteristics as portions of the control system are varied. Simulations performed using MATLAB with the different controller settings are compared to the experimental forced response results, as a method of prediction and result validation.

Chapter 5 reviews the experiments performed and the experimental results obtained, including the accuracy of the model in predicting the forced response of the system. We discuss the effects of controller parameter variation on rotor performance.

Chapter 6 makes conclusions about the accuracy of the model, the effects of a general PID controller, and the changes made in the control program. It also makes several recommendations about the work performed in this study, the usefulness of the controller gains in relation to rotor performance, and discusses other work that could be performed, including advanced control techniques.

Chapter 2: Rotor/Bearing System

2.1 Magnetic Suspension

The description of the magnetic suspension device in Fig. 2.1 is an excellent precursor to the explanation of magnetic bearing operation.

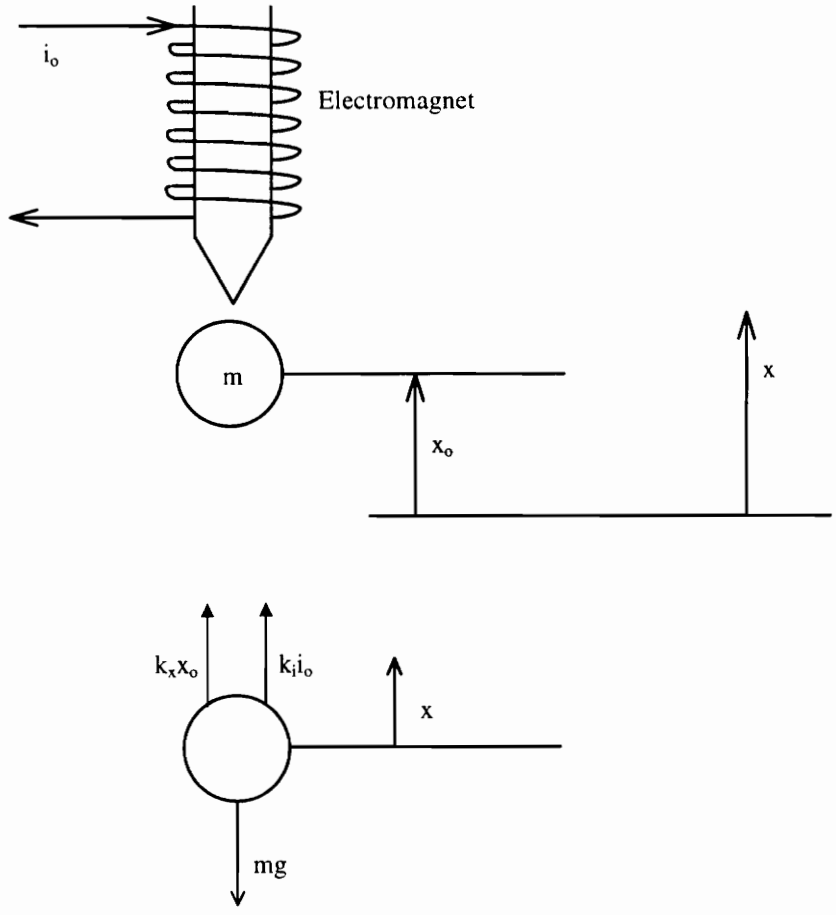

Figure 2.1

Magnetic Suspension Device and Free Body Diagram

Looking at the free body diagram of the magnetic suspension device, the force exerted on the ball by the magnet is a function of both the current in the coil and the ball's displacement. At a certain current 'i_o' and a certain position 'x_o', the magnetic forces due to the current and the position just balance the weight of the ball, or:

$$\Sigma F_x = -mg + f(x_o, i_o) = m\ddot{x} = 0$$

$$\Sigma F_x = -mg + k_x x_o + k_i i_o = m\ddot{x} = 0 \qquad (2.1)$$

where k_x and k_i are the linear constants relating force to displacement and force to current respectively. It must be noted here that these relationships are actually nonlinear and that linear behavior in a device such as this occurs within the operating range of both current and position. The plots in Fig. 2.2a and Fig. 2.2b show these relations well. The balance in equation (2.1) must be maintained for the ball to be stably suspended. However, if the position or current deviate from this "operating point", the ball drops from levitation. This can be shown in the following equations, letting $x_1 = x_o + \delta x$, where δx is the position deviation from the operating point:

$$\Sigma F_x = -mg + k_x(x_o + \delta x) + k_i i_o = m\ddot{x} \neq 0$$

$$\Sigma F_x = (-mg + k_x x_o + k_i i_o) + k_x \delta x = m\ddot{x} \neq 0 \qquad (2.2)$$

We know that the quantity in parentheses in equation (2.2) is equal to zero from equation (2.1), so the net force at this new point $x_1 = x_o + \delta x$ is not equal to zero. Since the forces no longer balance, the ball will accelerate in the direction of positive 'x', increasing the quantity δx, so that the net force gets larger, increasing δx even more, and the ball's displacement becomes unstable. To model the system in transfer function form, we make

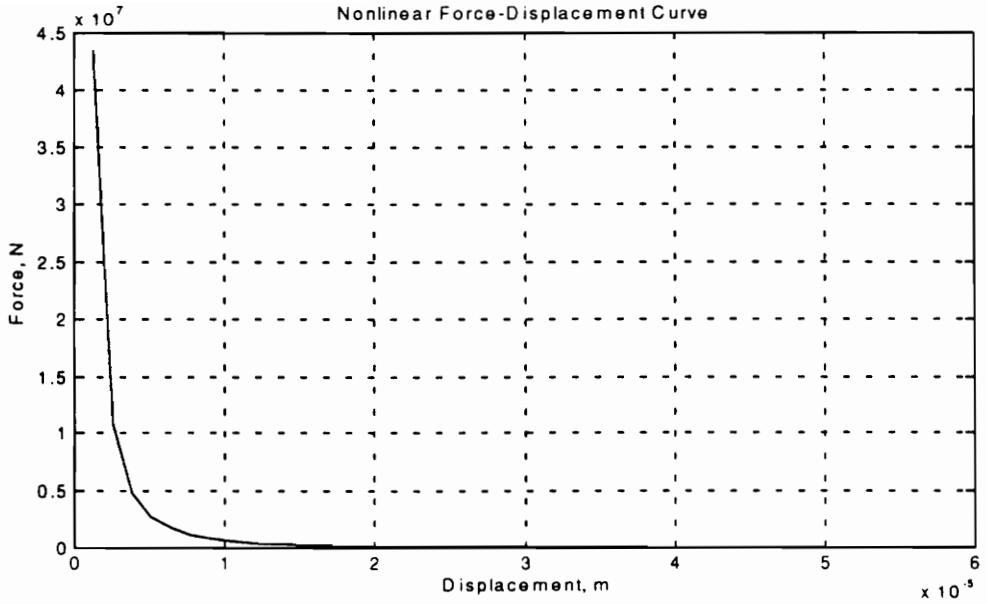

(a)

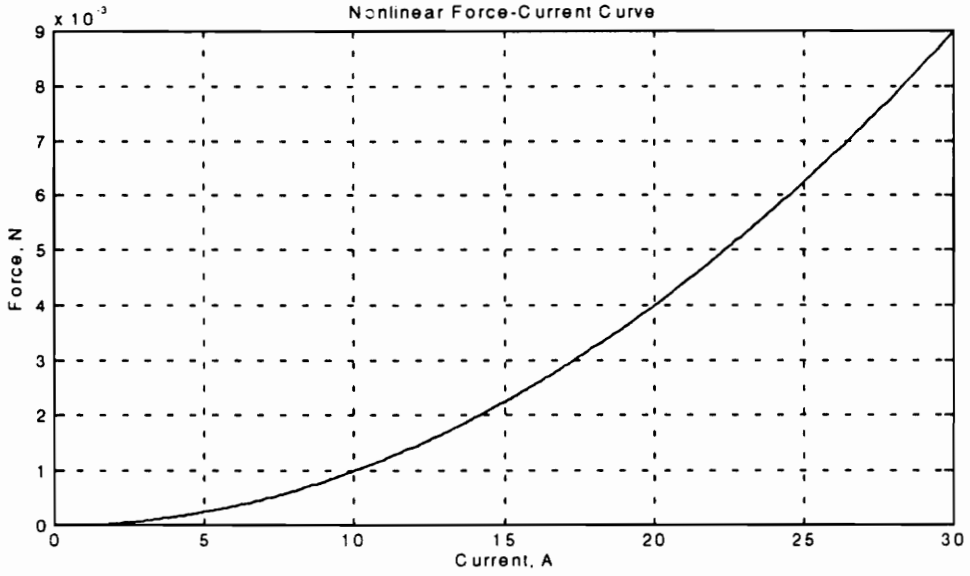

(b)

Figure 2.2: (a): Nonlinear Force-Displacement Curve; (b) Nonlinear Force-Current Curve

the assumption of linearity for the model of the force exerted on the ball by the magnet, expressed in the following equation, similar to equation (2.1):

$$f(x,i) \approx k_x x + k_i i \tag{2.3}$$

This derivation of this linearization is shown in Appendix A.1. The equation of motion changes to the following:

$$\Sigma F_x = -mg + k_x x + k_i i = m\ddot{x} \tag{2.4}$$

From equation (2.4), if we formulate a Laplace domain model of this system based on the Laplace transform of the position and current, we obtain the following equation:

$$\Sigma F_x = -mg + k_x X(s) + k_i I(s) = ms^2 X(s) \tag{2.5}$$

Rearranging terms results in the following transfer function:

$$\frac{X(s)}{k_i I(s) - mg + F_{ext}} = \frac{X(s)}{U(s)} = \frac{1}{ms^2 - k_x} \tag{2.6}$$

according to the following block diagram:

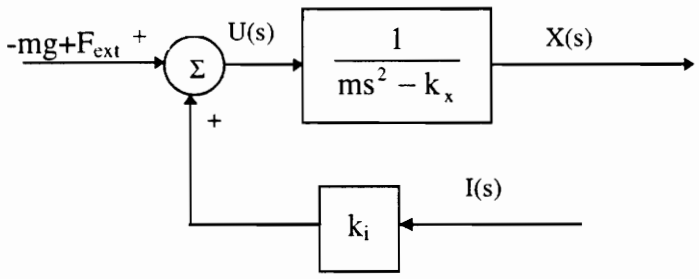

Figure 2.3: Open Loop Block Diagram of Magnetic Suspension System

The characteristic equation of this transfer function reveals the instability of this system. A positive eigenvalue of $+\sqrt{\frac{k_x}{m}}$ confirms our suspicion of instability. To stabilize this suspension device, we need to implement active control of the current in the wire coil. To do this, we can make the magnet current dependent upon the position of the ball, as in Fig. 2.4, moving the system's eigenvalues to stable locations.

This system can be considered a model of a single magnetic bearing because without control, like this suspension device, magnetic bearings attract the supported shaft in an unstable manner; thus like this device, magnetic bearings require feedback control to regulate the force that they exert on the shaft. In the following chapter, we will

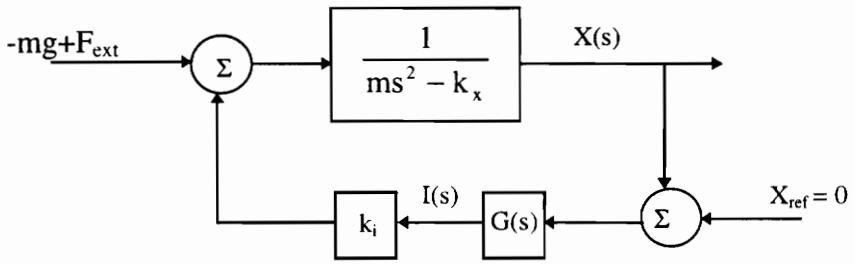

Figure 2.4: Block Diagram of Controlled Magnetic Suspension System

demonstrate how to design the control system transfer function G(s) to stabilize the magnetic suspension system and make the analogy between this design procedure and the design for a magnetic bearing control system.

2.2 Test Rig Description and System Model

The magnetic bearing test rig at the Rotor Dynamics Laboratory consists of three main components: the motor which drives the rotor at speeds up to 8000 RPM; the rotor, a 3-disk rotor supported at two ends by magnetic bearings; and the control system, which governs the current supplied to the bearings and thus governs the forces applied by the bearings on the shaft. The diagram in Fig. 2.5 gives an idea of the configuration of the magnetic bearing test rig. This section will describe the characteristics of the rotor and control system. We will also present a finite element model of the rotor and a model of the control system transfer function.

It is useful to describe the operation of the rotor to get an idea of the interaction of the control system and rotor in a qualitative sense. We will first describe the action of levitating the rotor without spinning, then the action during normal running of the rotor.

When the rotor is simply levitated by the bearings, the force being supplied by the bearings is constant, which means that the current supplied to the bearings is constant as well.. Since the rotor is not spinning, no whirl or vibration is taking place, so the output of the position sensors which monitor the motion of the rotor does not change. This means that the current supplied to the bearings is constant. The constant currents in the

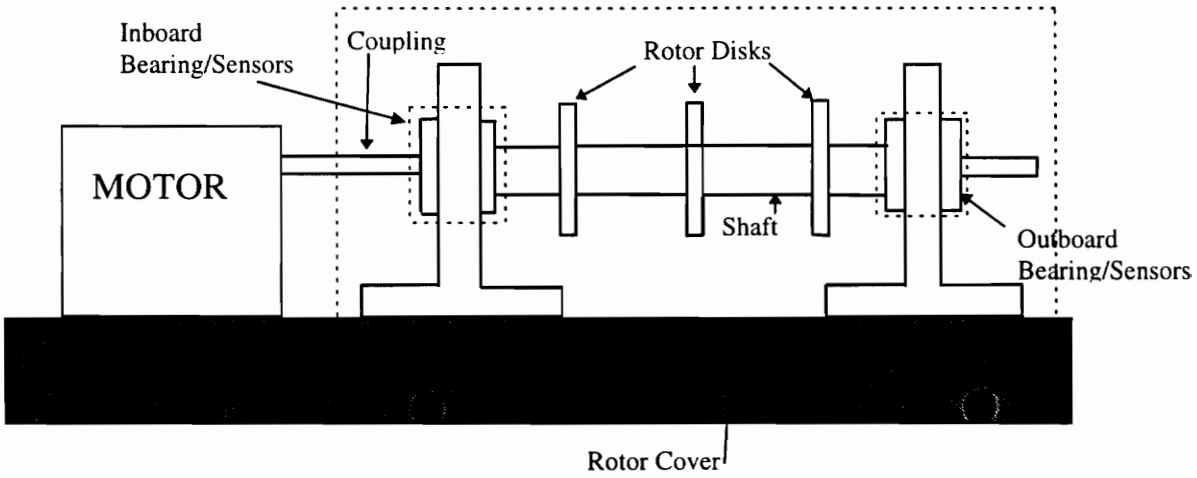

Figure 2.5: Magnetic Bearing Test Rig

bearings which support the weight of the rotor is referred to as the bias current, which wil lbe explained in a later section.

As the rotor spins about its geometric axis, driven by the 200 HP motor, position sensors produce a voltage in proportion to the rotor's whirl amplitudes. This voltage is sent to the control system, which processes the signal according to its pre-programmed algorithm, then sends a control voltage to the power amplifiers. These amplifiers produce a control current in proportion to the control voltage; this current drives the magnetic bearings, which produce force in proportion to the current. The current supplied to the bearings now consists of the constant or bias current which levitates the rotor at zero spin speed and the control current based on the whirl of the rotor. The bearing force regulates the position of the rotor at the bearings, constraining the whirl amplitude of the rotor to reasonable levels. The magnetic bearing control system contains five independent axes of control, one thrust axis and four radial axes, so four different independent radial forces are applied to the rotor by the bearings.

2.2.1 Rotor Description and Model

Currently the magnetic bearing test rig is used to support a stainless steel rotor which has three external disks attached symmetrically between the bearings. The entire rotor (including disks) is 63.58 inches long and weighs 440 lbs. The external disks have a diameter of 8 inches and are 2.5 inches wide. Each disk is tapped with 36 circumferential holes which are used for balance weights. In addition to the external

disks on the rotor, landing sleeves which are used for rotor drops onto the backup bearings are mounted outboard of the magnetic bearings on the shaft.

The motor is driven by a 200 HP test stand motor, currently capable of driving the rotor to speeds up to 8000 RPM. The rotor and motor connect through a dry flexible coupling.

The finite element method is easily applied to the modelling of rotors. Discretizing the rotor into a finite number of masses with massless elastic connectors, we determine the stiffnesses of the connectors to both translational and angular displacements. Writing equations of motion for each degree of freedom (two translational and two angular displacements at each discrete mass or station) and regrouping them into matrix form, we form the mass and stiffness matrices. The matrix of terms dependent upon rotational and translational velocities, which can be considered a matrix of damping terms, is formed by accounting for gyroscopic moments in the rotor. Writing the equations in matrix form:

$$[M][\ddot{z}]+\omega_S[G][\dot{z}]+[K][z]=[f_{ext}] \qquad (2.7)$$

where 'z' represents the vector of coordinates along the rotor (seen in equation 2.7), ω_s is the spin speed of the rotor, [G] is the skew-symmetric gyroscopic matrix and $[f_{ext}]$ is a vector of external forces such as rotating unbalances. From this point onwards we will refer to the product $\omega_s[G]$ as the rotor damping matrix, [C].

$$z=\begin{bmatrix} x_1 \\ y_1 \\ \theta_{x1} \\ \theta_{y1} \\ x_2 \\ . \\ . \\ \theta_{y19} \\ x_{20} \\ y_{20} \\ \theta_{x20} \\ \theta_{y20} \end{bmatrix} \tag{2.8}$$

The model used in this thesis consists of twenty stations, which equates to 80 degrees of freedom. A graphical representation of the rotor model can be seen in Fig. 2.6. A flexible coupling connects the rotor to the motor, and is modelled as an external mass at the inboard end of the rotor, as seen in the figure. Also note the location of the magnetic bearings denoted with a '**B**', and the accompanying sensors, denoted with an '**P**', at stations 6 and 15. Probes are also present in the model at stations 3 and 18, which are the bearing landing sleeve locations.

2.2.2 Control System/Rotor Interaction

Before proceeding to an explanation of the components of the control system, it is informative to explain the interaction of the control system and the rotor by means of a block diagram, seen in Fig. 2.7:

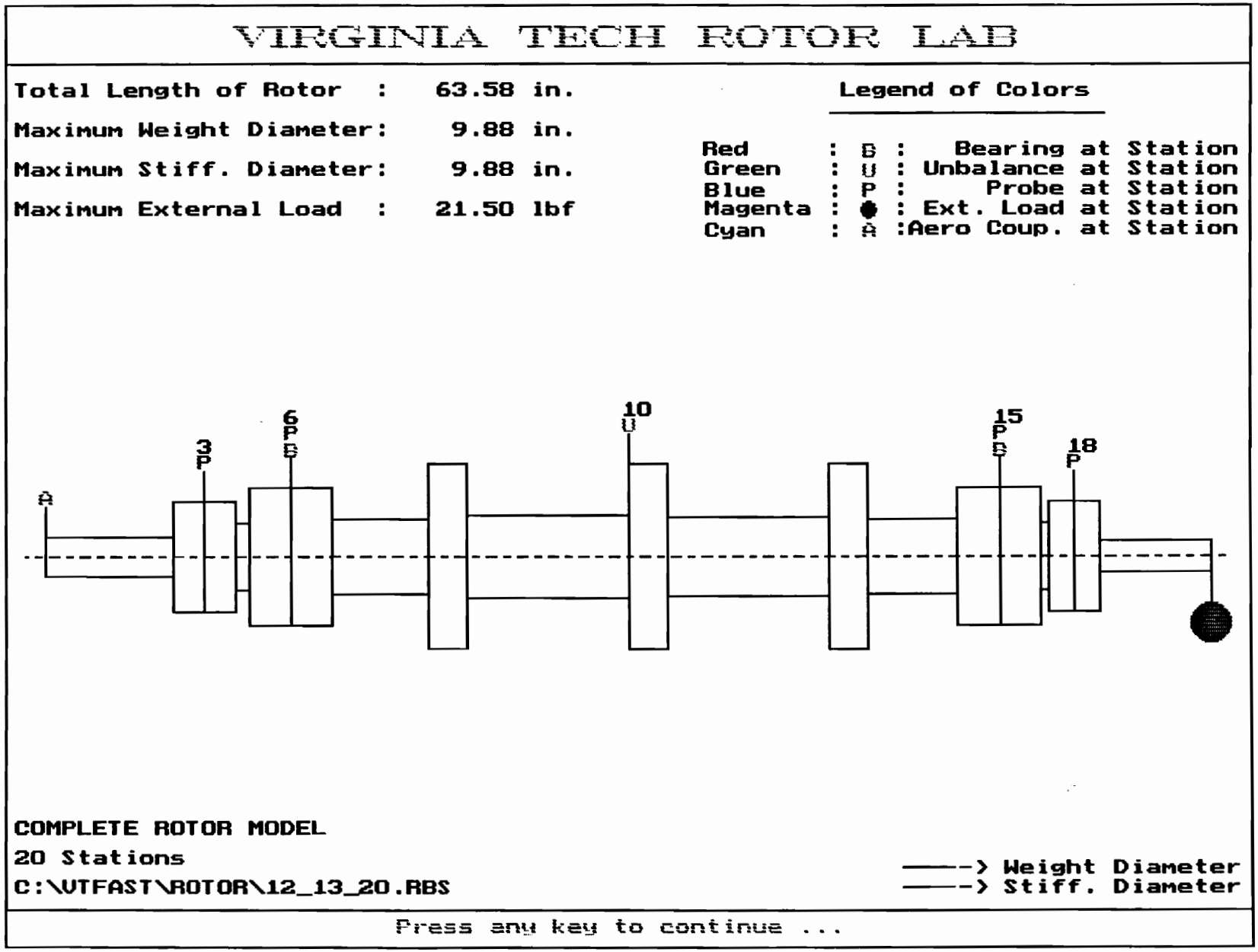

Figure 2.6: Diagram of Rotor Model

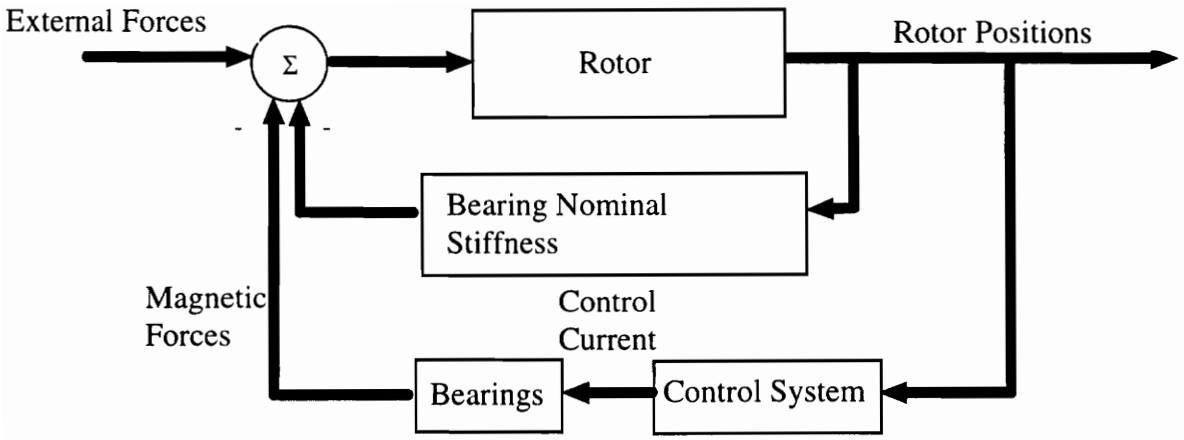

Fig. 2.7: Conceptual Block Diagram of Rotor-Bearing System

As seen in the block diagram, the radial displacements at the sensor locations are used for feedback to the control system, from which a control current is generated in the magnetic bearings, which exert a force on the rotor in proportion to the current. Also, the block diagram includes a feedback loop for the nominal attractive stiffness of the bearings; this feedback is implicit in the bearings.

2.2.3 Control System Description

The current control system is housed in a control cabinet donated by Societe de Mechanique Magnetique (S2M). The control algorithm programmed on the Digital Signal Processor Boards applies a PI (Proportional-Integral) algorithm to the output of the position sensors, and sends a control voltage to the power amplifiers, which produce currents to regulate the motion of the rotor. A detailed model must account for all the electrical components present in the feedback loop to produce an accurate representation

of the control system. Figure 2.8 expands on the control system block of Fig. 2.7. Following the path of the control loop in Fig. 2.8, the following sections explain the characteristics of the components of the control algorithm used in the feedback loop.

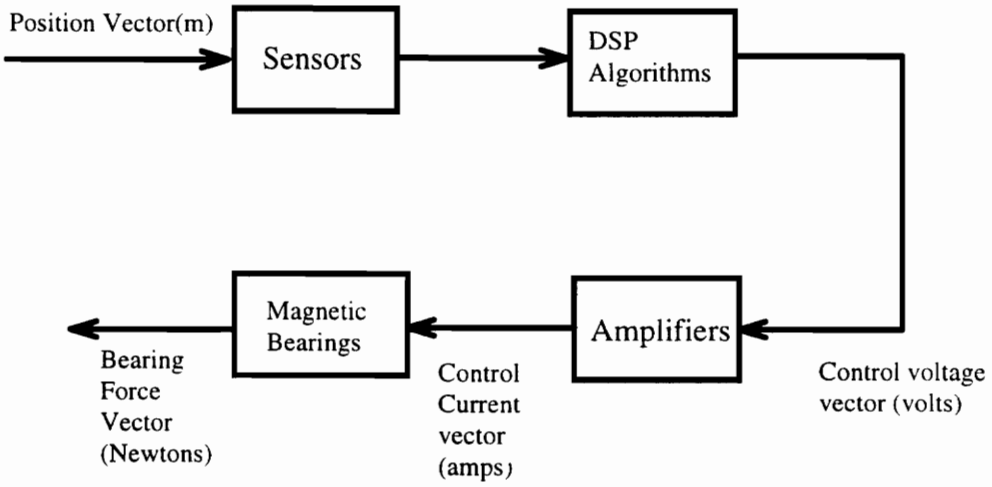

Fig. 2.8: Control Block Diagram for Magnetic Bearing Control System

2.2.4 Position Sensors

As the rotor runs under power from the motor, inductance position sensors produce voltage in proportion to the rotor's radial position. There are five sensors, four measuring radial position at the four radial magnetic bearings, and the fifth measuring the

axial position of the rotor. The radial sensors at the bearings are configured as in Fig. (2.9) :

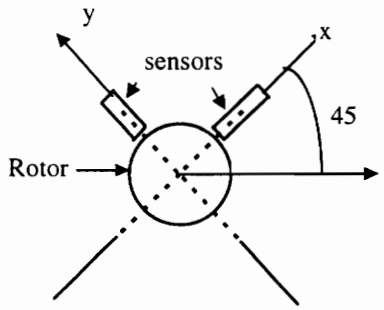

Fig. 2.9 : Radial Sensor Configuration

The sensors are configured in this way for the bearings at both ends of the rotor (inboard and outboard ends). Calibrated so that zero voltage results from zero position (i.e. no whirl is taking place), the sensors' output is a 17 KHz amplitude modulated signal. The gain of the sensors is, in English units, 600 mV/mil, or 600 millivolts per thousandth of an inch. Converted to SI units, the sensor sensitivity becomes 23600 Volts / meter. Thus we can represent the sensor transfer function as a gain with infinite bandwidth, as follows:

$$G(s)_{sensor} = 23600 \text{ V/m} \tag{2.9}$$

The demodulator boards accept the sensors' outputs and converts them to analog position signals, an appropriate form for the DSP board to process.

2.2.5 Main Control System

The following block diagram expands on Fig. 2.8 by showing all the blocks contained in the DSP board's portion of the control loop in Fig. 2.8:

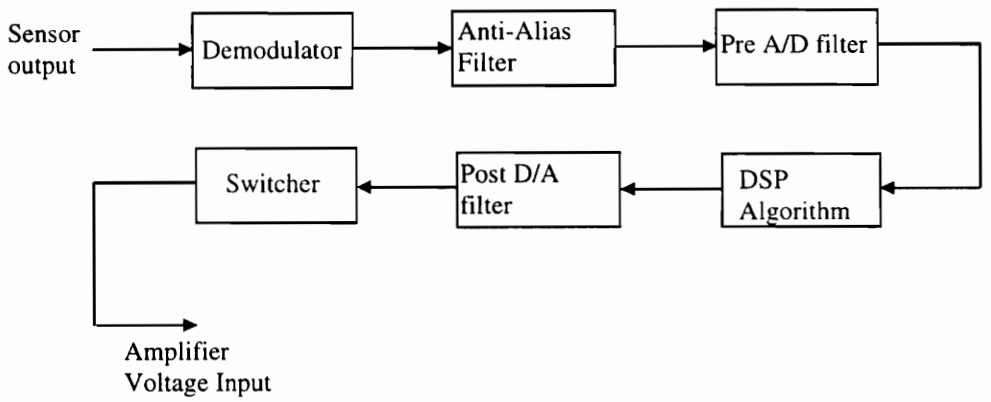

Fig. 2.10: Expanded Block Diagram of DSP Algorithm

S2M provides a subroutine which calculates the frequency response of the portion of the control loop from the input of the demodulator to the output of the switcher. The demodulator card's function is to convert to the amplitude modulated sensor output voltage into an analog position signal. From the subroutine provided by S2M, the zero order hold across the demodulator can be represented by the following gain and phase

$$\text{Gain} = 34000\sqrt{\frac{2-2\cos(\frac{\omega}{34000})}{\omega^2}} \text{ V/V} \tag{2.10}$$

$$\text{Phase} = \tan^{-1}\left[\frac{\sin(\frac{\omega}{34000})}{1-\cos(\frac{\omega}{34000})+10^{-6}}\right] - \frac{\pi}{2} \text{ (radians)} \tag{2.11}$$

where 'ω' is the frequency of the input signal.

The output of the demodulator board goes to the anti-alias filter, which is set up to prevent aliasing of the signal to be sampled by attenuating high frequency content in the signal. The transfer function of the anti-alias filter is:

$$G_{aa}(s) = \frac{(10000\pi)^2}{s^2 + 2(0.32)(10000\pi)s + (10000\pi)^2} \tag{2.12}$$

After passing through the anti-alias filter, the signal proceeds to the pre A/D filter, a first order filter which attenuates very high frequencies. The transfer function of the pre A/D filter is:

$$G_{pad}(s) = \frac{(18555 \cdot 2\pi)}{s + 18555 \cdot 2\pi} \tag{2.13}$$

At this point the signal enters the DSP board. First it is sampled from an analog signal to a discrete signal, then the board receives the signal and processes it through a chain of different discrete control algorithms, whose discrete transfer functions are shown in the

table below. The coefficients of the transfer functions in table 2.1 are those programmed during the most recent controller retuning by S2M, in August of 1995:

Table 2.1: Discrete Control Algorithms of DSP Board

Algorithm	Discrete transfer function
Bandwidth Filter	$G_{bw}(z) = \frac{-1.7684z^2}{z^2 - 0.8801z + 0.5874}$
Phase Lead Cells	$G_{pc}(z) = \frac{8.0515z^2 - 15.22z + 7.1755}{z^2 - 1.7009z + 0.70783}$
Integrator	$G_{int}(z) = \frac{0.0052261z}{z - 1}$
Notch Filter # 1	$G_{n1}(z) = 1$
Notch Filter # 2	$G_{n2}(z) = 1$
Phase Bump	$G_{pb}(z) = \frac{1.299z^2 - 2.4101z + 1.1499}{z^2 - 1.8465z + 0.88522}$

The block diagram of these filters on the DSP board is arranged as follows:

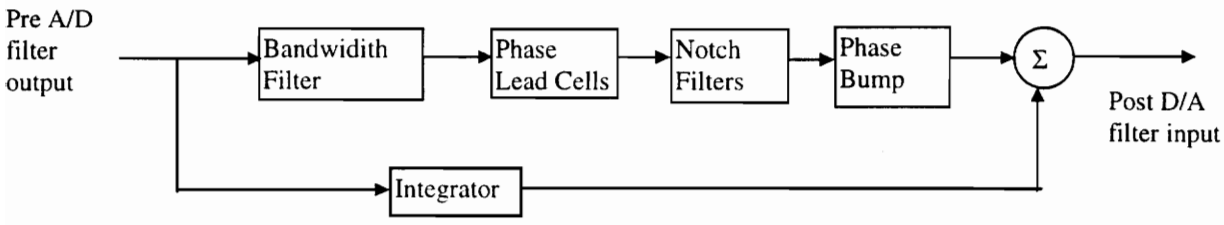

Fig. 2.11 : Block Diagram of DSP Board Algorithm

The coefficients of the transfer functions are calculated using the user-entered values for various values such as proportional gain, integral gain, notch filter frequency, etc. The transfer functions are shown in frequency response form in Fig.s 2.12 through 2.14. Since the notch filters were deactivated in the last tuning, a sample notch filter at 200 Hz was generated and is shown with the other plots. Also, due to delays caused by conversion and processing in the control loop, a phase loss occurs and is represented by the following equation:

$$P_{loss} = \frac{\omega}{2\pi}(20)(10^{-6})(360), \text{radians} \tag{2.14}$$

After the DSP board processes the signal, the output is then converted back to an analog signal, and the post D/A filter operates on it. The transfer function of the post D/A filter is:

$$G_{pda}(s) = \frac{(16000 \cdot 2\pi)}{s + 16000 \cdot 2\pi} \tag{2.15}$$

The digital switcher board converts this post D/A filter output signal from bipolar (-15V to +15V) to unipolar (0 to 10V) for amplifier operation. The gain and phase of the zero order hold across the digital switcher board can be represented as follows:

$$\text{Gain} = 17000\sqrt{\frac{2 - 2\cos(\frac{\omega}{17000})}{\omega^2}} \quad \text{(V/V)} \tag{2.16}$$

$$\text{Phase} = \tan^{-1}\left[\frac{\sin(\frac{\omega}{17000})}{1 - \cos(\frac{\omega}{17000}) + 10^{-6}}\right] - \frac{\pi}{2} \quad \text{(radians)} \tag{2.17}$$

where 'ω' is the signal frequency.

The output of the switcher board is the control voltage and is sent to the power amplifiers, which generate the current in the magnetic bearings. The two options which exist for the type of amplifier operation are Class A and Class B. The current control system is running Class B control, meaning that only the upper of the two electromagnets in each control axis is energized and produces force.

In keeping with the notation of the chapter, we will represent the entire transfer function of the main control system as G_c, which accounts for all the components in this section from the input of the demodulator to the output of the switcher. Although the DSP portion of the loop is in discrete form, we combine this portion with the continuous representation of the other filters in the loop to perform a frequency analysis. The program provided by S2M allows the calculation of the frequency response of this transfer function. In the next chapter, we will show experimental verification of this frequency response.

2.2.6 Amplifier Characteristics

The amplifiers receive a control voltage from the DSP boards (by way of the digital switcher card) and generate the control current in the magnetic bearings. The current to voltage ratio that the amplifiers produce is 1.5 Amps/Volt.

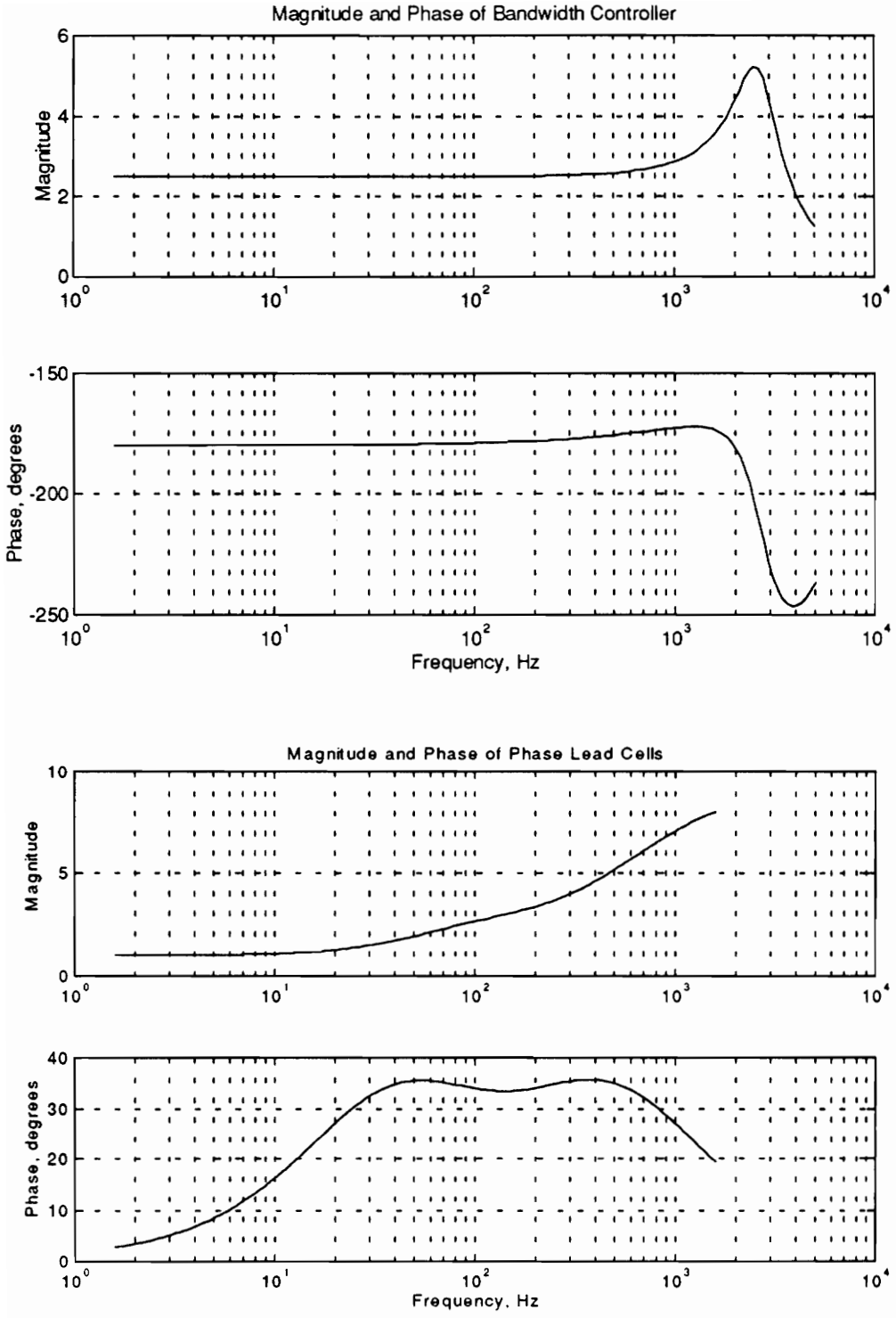

Fig. 2.12: Bode Plots of Bandwidth Controller and Phase Lead Cells

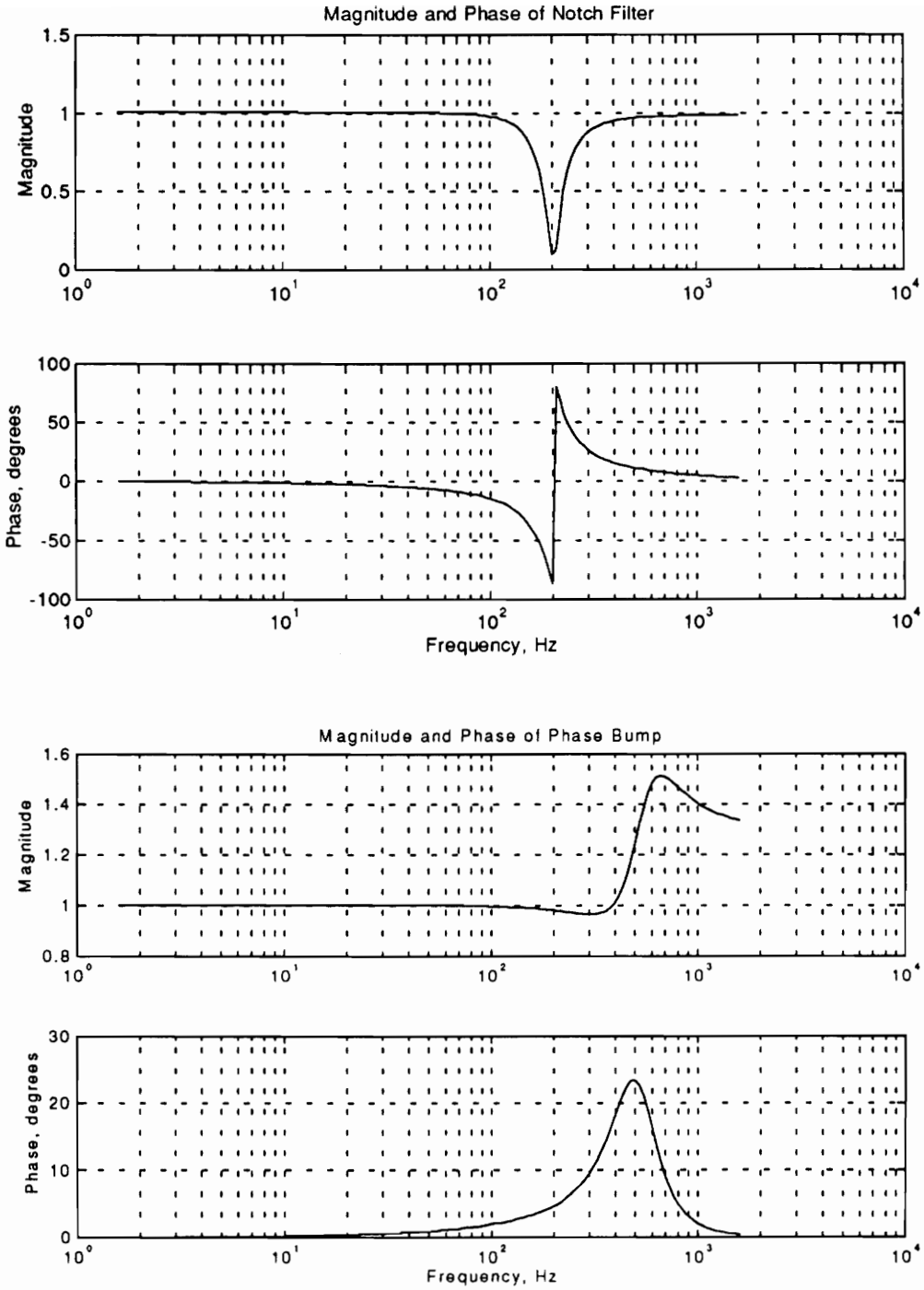

Fig. 2.13: Bode Plots of Notch Filter and Phase Bump Filter

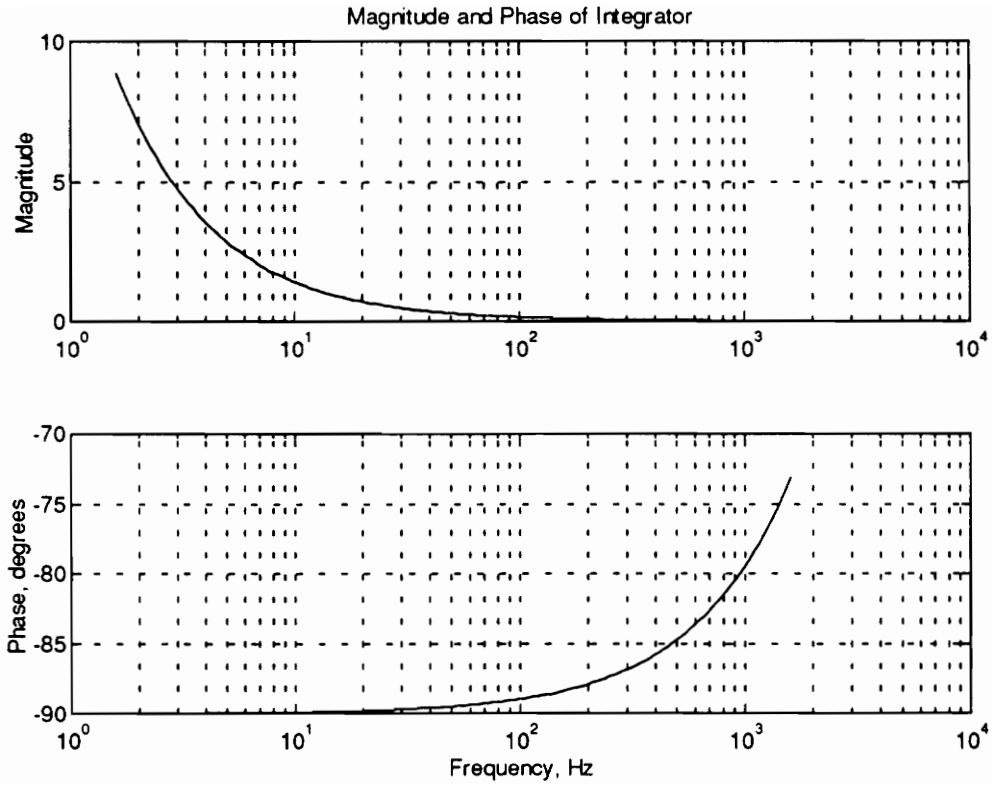

Fig. 2.14: Bode Plot of Integrator

This amplifier gain of 1.5 will be used in all calculations of the effective stiffness and damping of the control loop. The transfer function of the amplifier can be modelled as a simple gain, as follows:

$$G_{amp} = 1.5 \quad A/V \tag{2.18}$$

2.2.7 Bearing Model

The last portion of the control system feedback loop is the magnetic bearings, which produce a force as a function of the current generated in the wire coils by the amplifiers. As mentioned with the suspension device, the relationship between the force produced by the bearings and the current in the coils is nonlinear; force is proporitional to the square of the current. However, we make the assumption of linearity around the bias current during normal operation. The drawing in Fig. 2.15 shows the configuration of the magnetic bearings with respect to the shaft. Both the inboard and outboard magnetic bearings are configured in this fashion.

When the rotor is levitated but not spinning, the position of the shaft is constant (at or close to zero with respect to the rotor's geometric axis) and the current produced by the amplifiers to keep the shaft levitated is also constant. This constant current is known as *bias current* and is the point around which the force-current sensitivity is linearized, and also the point about which the equations of motion for the rotor are written.

As with a spring-mass system where the equations of motion are written about the spring's static displacement, the equations of motion for our system are written about the bias current. This allows us to neglect gravity in our modelling procedure, because the force provided by the bias current in the bearings levitates the rotor at zero spin. Linearizing the force-current relationship leads to representing the relation as a gain, usually known as k_i. The force-current relation, or current stiffness, is a function of the bearing characteristics and can be represented as equation 2.19:

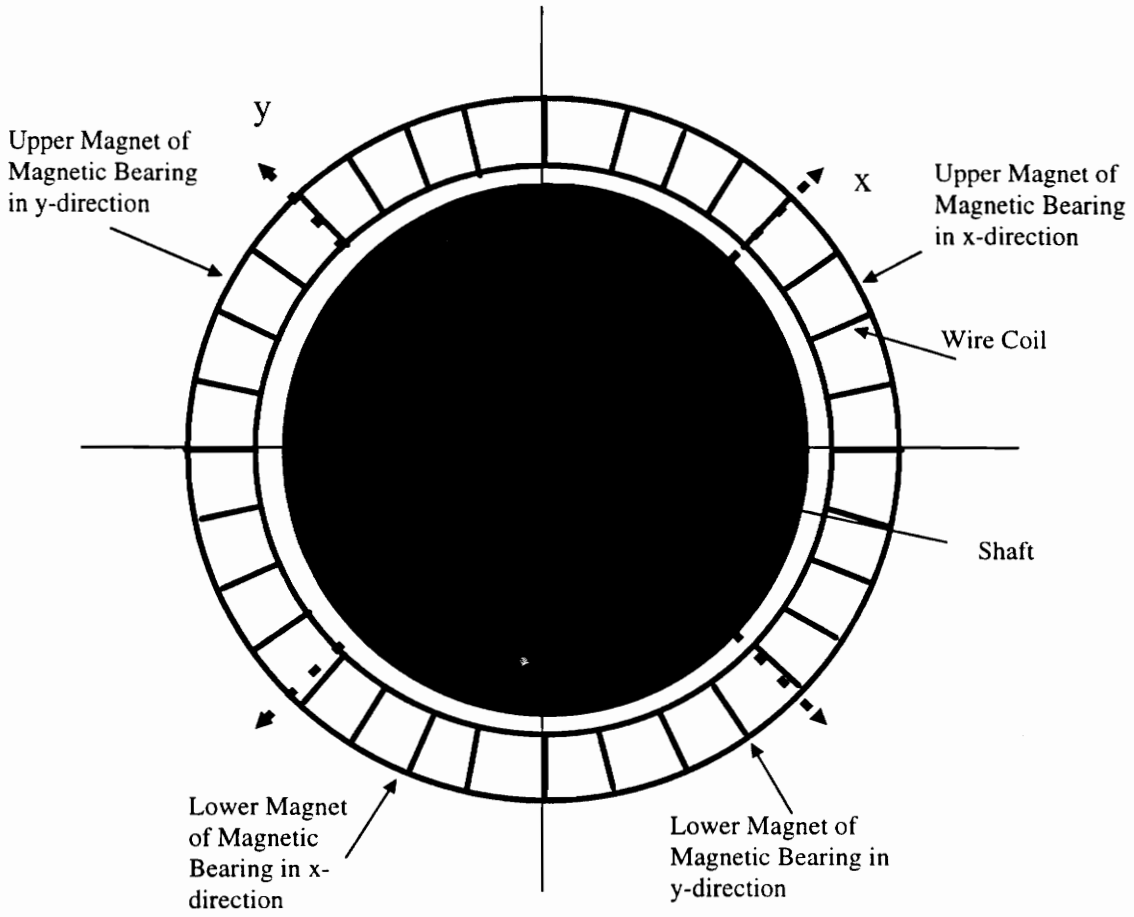

Fig. 2.15: Magnetic Bearing Configuration

$$k_i = \frac{2\mu_o A_g N^2 I_b}{G^2} \quad \text{N/A} \tag{2.19}$$

where:

μ_o = permeability of free space

A_g = projected magnet area

N = number of coils per magnetic pole pair

I_b = bias current in bearing

G = nominal air gap

The derivation of this expression is shown in appendix A.1. In our magnetic bearing test rig, the two magnetic bearings possess different values of k_i due to different geometry. Specifically, the projected area at the inboard bearing is larger than the projected area at the outboard bearing. The plots in Fig. 2.16, which are the force-current relationships for the inboard and outboard bearing respectively, clearly show two things: the nonlinearity in the force-current relationships and the larger forces produced by the inboard bearing. The bias currents in each control axis, summarized in the table below, clearly fall in the linear range in the figures.

Table 2.2: Bearing Characteristics

Axis of Control	Bearing	Force-Current Coefficient (N/A)	Bias Current (Amps)
V13 (x-axis)	Outboard	296.67	10.5
W13 (y-axis)	Outboard	296.67	10.5
V24 (x-axis)	Inboard	356	11.0
W24 (y-axis)	Inboard	356	11.0

The slopes of the plots at the bias current level of bearing current correspond to the force-current relationship for the bearing, k_i

2.2.8 Summary of Control Loop

The entire control loop takes a position signal and produces a force on the bearing; thus the units of the control loop transfer function are force per unit length. The sensors produce a voltage in proportion to the position deviation of the rotor, which is sent to the DSP boards. There a pre-programmed algorithm operates on the signal, and the board send their output to the amplifiers. The amplifiers receive the voltage, then produce and send a current to the magnetic bearings, which produce forces to keep the rotor on line. To accurately model the control system, we produce the following transfer function:

$$G_{cs}(s)=G_s(s)G_c(s)G_a(s) \tag{2.20}$$

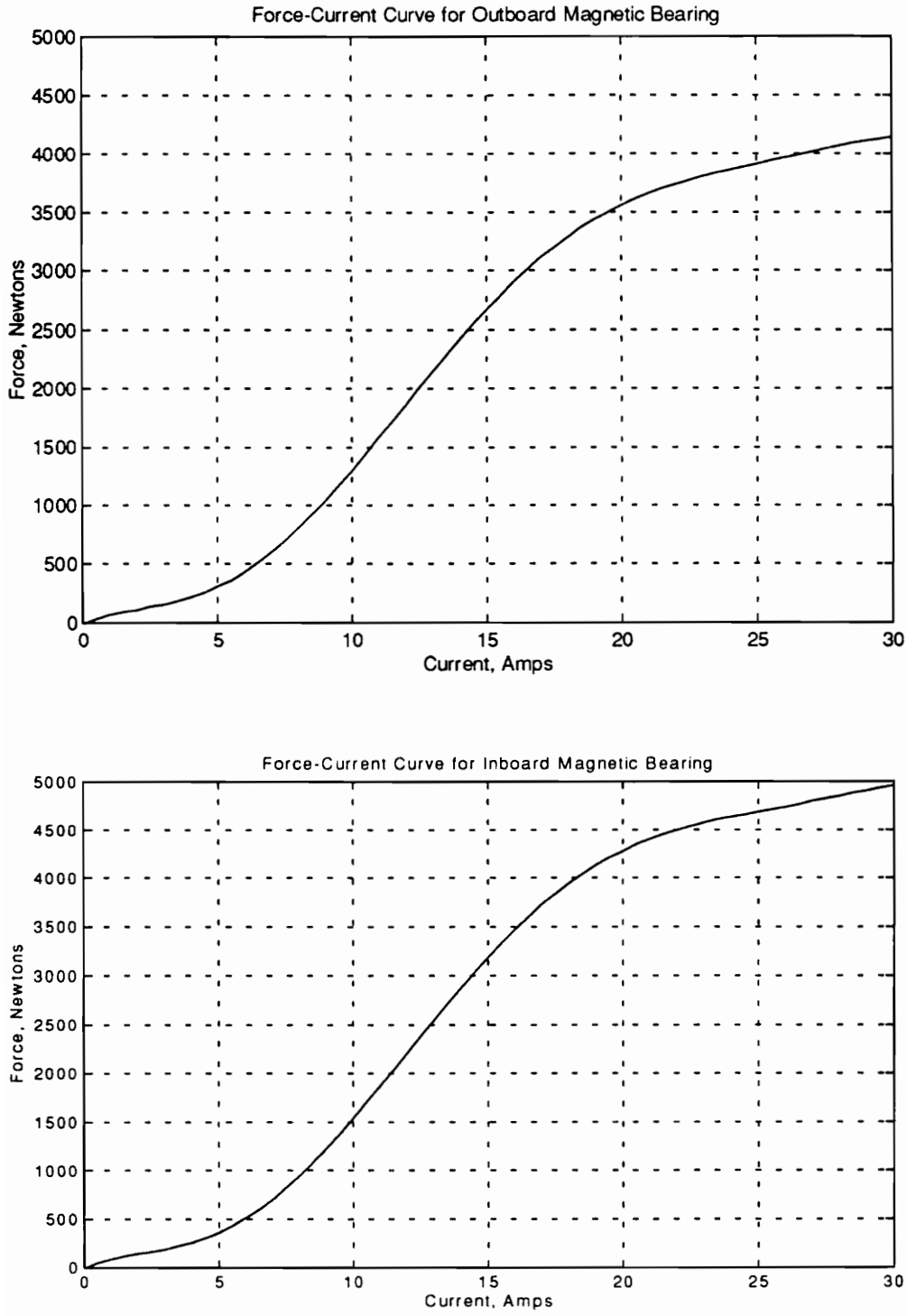

Fig. 2.16: Inboard and Outboard Bearing Force-Current Curves

Since all four radial sensors have the same gain, each control axis is tuned identically, and the amplifiers have the same characteristics, this transfer function is the same for all four radial axes of control. However, since the force-current relation for the inboard bearing is larger than for the outboard bearing, the forces produced for the two inboard axes are larger than those produced for the two outboard axes.

2.3 Chapter Summary

This chapter has introduced the concept of magnetic suspension, and shown the uncontrolled instability of these systems. We have presented a finite element model for the rotor, based on twenty mass elements, and we have described the physical characteristics of the rotor and external masses. We have summarized the control loop which runs on the magnetic bearing system, including the discrete and continuous transfer functions where appropriate.

The following chapter discusses the general need for control outlined above, how a control system affects a plant's dynamic properties, how we model a control system with a magnetic bearing system, and the effects of various controller parameters on controller and system properties. We also describe the tuning of the control system presently installed on the magnetic bearing test rig control cabinet, and how the parameters in this control system affect magnetic bearing properties.

Chapter 3: Controller Theory and Design

3.1: Control requirement

It is evident from the model of the suspension device in the previous chapter that this and other magnetic devices such as magnetic bearings are inherently unstable, so we must control the rotor's position through feedback for stabilization. The following sections will describe the methods used to stabilize a magnetic bearing supported rotor and how these control methods affect bearing properties.

3.2 Controller Properties

For a simple system such as an actively controlled single-degree of freedom mass-spring-damper system, the effective dynamic properties of the system are influenced by the transfer function present in the feedback control loop. Looking at a feedback control loop for a second order damped system with G(s) as the feedback transfer function, in Fig. 3.1, we can form the closed loop transfer function with P(s) as the plant transfer function and G(s) as the feedback transfer function: $CLTF = \frac{P(s)}{1 + P(s)G(s)}$

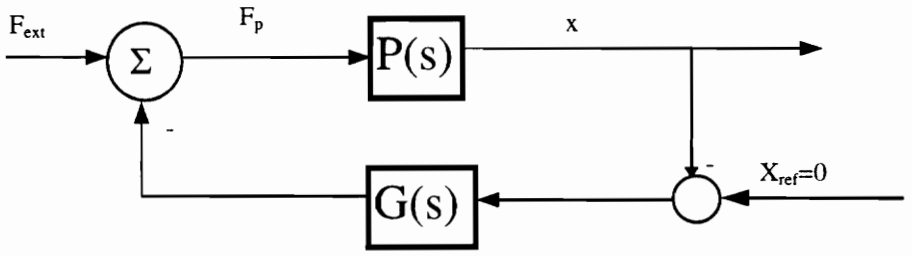

Figure 3.1: Feedback Control System of a General Plant P(s) and Feedback G(s)

Assume the model of the plant to be the following:

$$\frac{x(s)}{F_p(s)} = \frac{1}{ms^2+cs+k} = P(s) \tag{3.1}$$

where 'm' represents the mass, 'c' the damping value, and 'k' the stiffness value of the second order damped system as in Fig. 3.2.

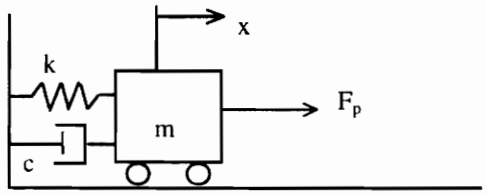

Figure 3.2: Spring-Mass-Damper System

The plant's input, 'F_p', is the control input and the plant's output,'x' is the position of the mass. Assuming feedback control as in Fig. 3.1, we see that the force input into the plant is function of both the external force input and the position feedback. Writing a loop equation for the plant's force input, and rearranging terms, we obtain:

$$F_p = F_{ext} - G(s)x \tag{3.2}$$

$$(ms^2 + cs + k)x = F_p = F_{ext} - G(s)x \tag{3.3}$$

$$(ms^2 + cs + k + G(s))x = F_{ext} \tag{3.4}$$

This gives us the closed loop transfer function:

$$\frac{x}{F_{ext}} = \frac{1}{ms^2 + cs + k + G(s)} \tag{3.5}$$

Denoting s=jω, taking the frequency response of (3.7), and rearranging terms, we get:

$$(-\omega^2 m + j(\omega c + Im(G(j\omega))) + (k + Re(G(j\omega)))X = F_{ext}(j\omega) \tag{3.6}$$

If we then view the imaginary quantity as an effective damping multiplied by frequency of harmonic excitation, and the real quantity as an effective stiffness, we can define these terms as the following:

$$k_{eff} = k + Re(G(j\omega)) \tag{3.7}$$

$$c_{eff} = c + \frac{Im(G(j\omega))}{\omega} \tag{3.8}$$

If we wish to add damping to the system without affecting the stiffness, derivative feedback ($G(s) = K_d s$, where K_d is a gain constant) which has a purely imaginary frequency response ($G(j\omega)=j\omega * K_d$), increases the system's damping by 'K_d' while leaving the stiffness unchanged. Similarly, proportional feedback ($G(s) = K_p$) which has a purely real frequency response, increasing the system's stiffness by 'K_p' while leaving the damping unchanged.

3.3 A Specific Controller: PID and its effect on dynamic properties

The classical continuous PID controller has the following transfer function:

$$G_{PID}(s) = K_p + \frac{K_i}{s} + K_d s \tag{3.9}$$

where K_p is the proportional gain, K_i is the integral gain, and K_d is the derivative or rate gain, and is commonly used in the control of magnetic bearing systems. It is therefore

useful to examine the effects that the PID parameters have on the dynamic properties of a controlled system. Assuming implementation of this controller in the same way as the controller G(s) in the previous section, and taking the frequency response as in the previous section, we get:

$$G_{PID}(j\omega) = K_p + j \cdot (\frac{-K_i}{\omega} + K_d\omega) \tag{3.10}$$

From looking at equation (3.10), we see that the dynamic stiffness of the PID controller is dependent upon the proportional gain, while the damping is a function of both the integral and derivative gain. In particular, the damping depends linearly upon the derivative gain, while the contribution from integral gain is negative, decreasing the damping, getting less and less negative (i.e. moving towards zero) as frequency of excitation increases. Integral control mainly rejects steady state error and has a small effect on the damping. Figures 3.4, 3.5, and 3.6 show the variation of stiffness and damping with frequency of excitation and PID controller gains. From the plots, we can conclude several things. First, as predicted, proportional gain affects only the controller stiffness, and has no effect on the damping. Secondly, derivative or rate gain affects only the damping and has no effect on the stiffness. Third, integral gain's effect on stiffness is extremely low, and while it does affect damping, the most significant contribution integral gain occurs at low frequencies, and as frequency increases, integral gain's contribution to controller damping falls off inversely proportional to frequency.

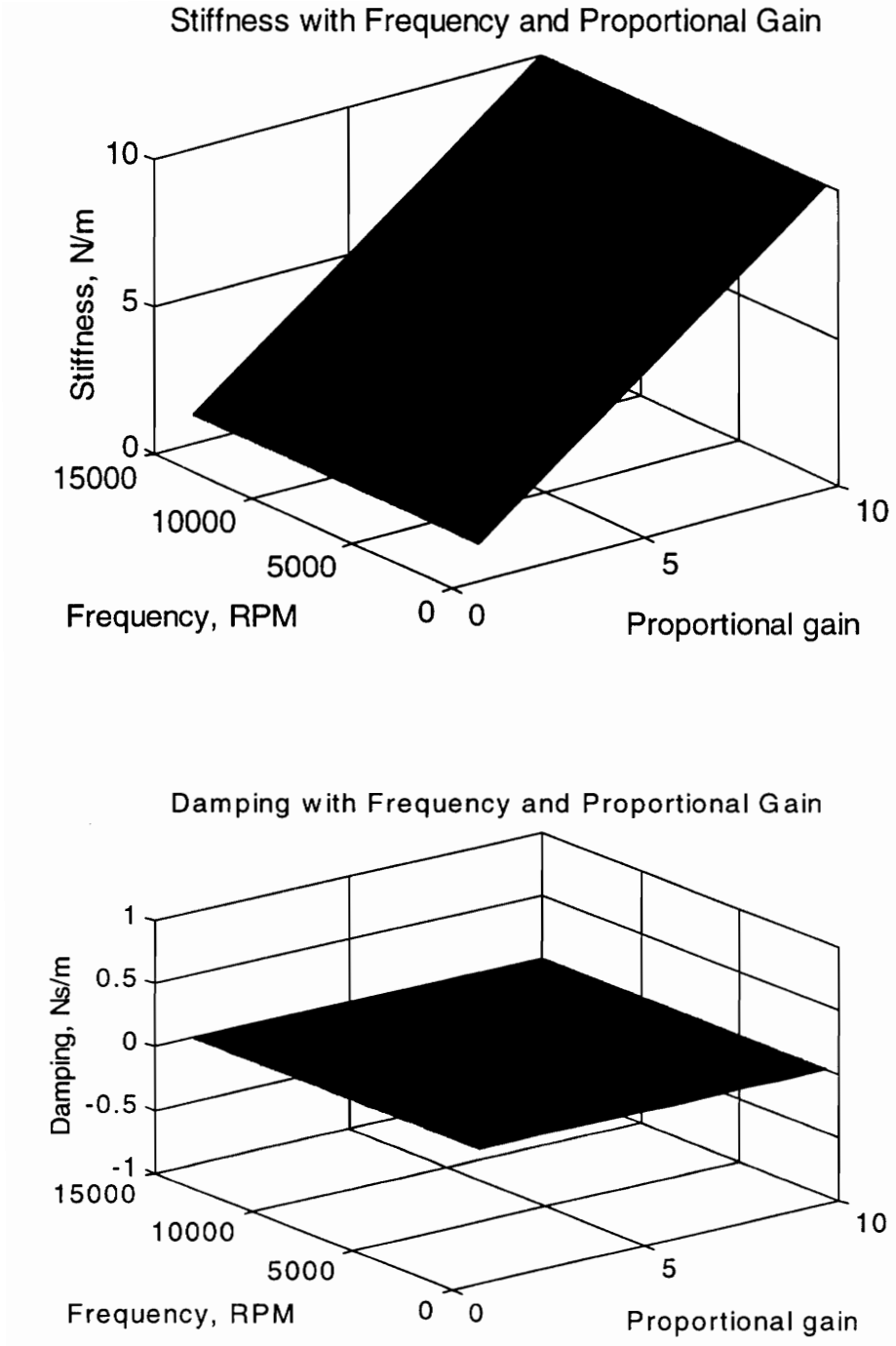

Figure 3.3: Variation of Stiffness and Damping with Proportional Gain

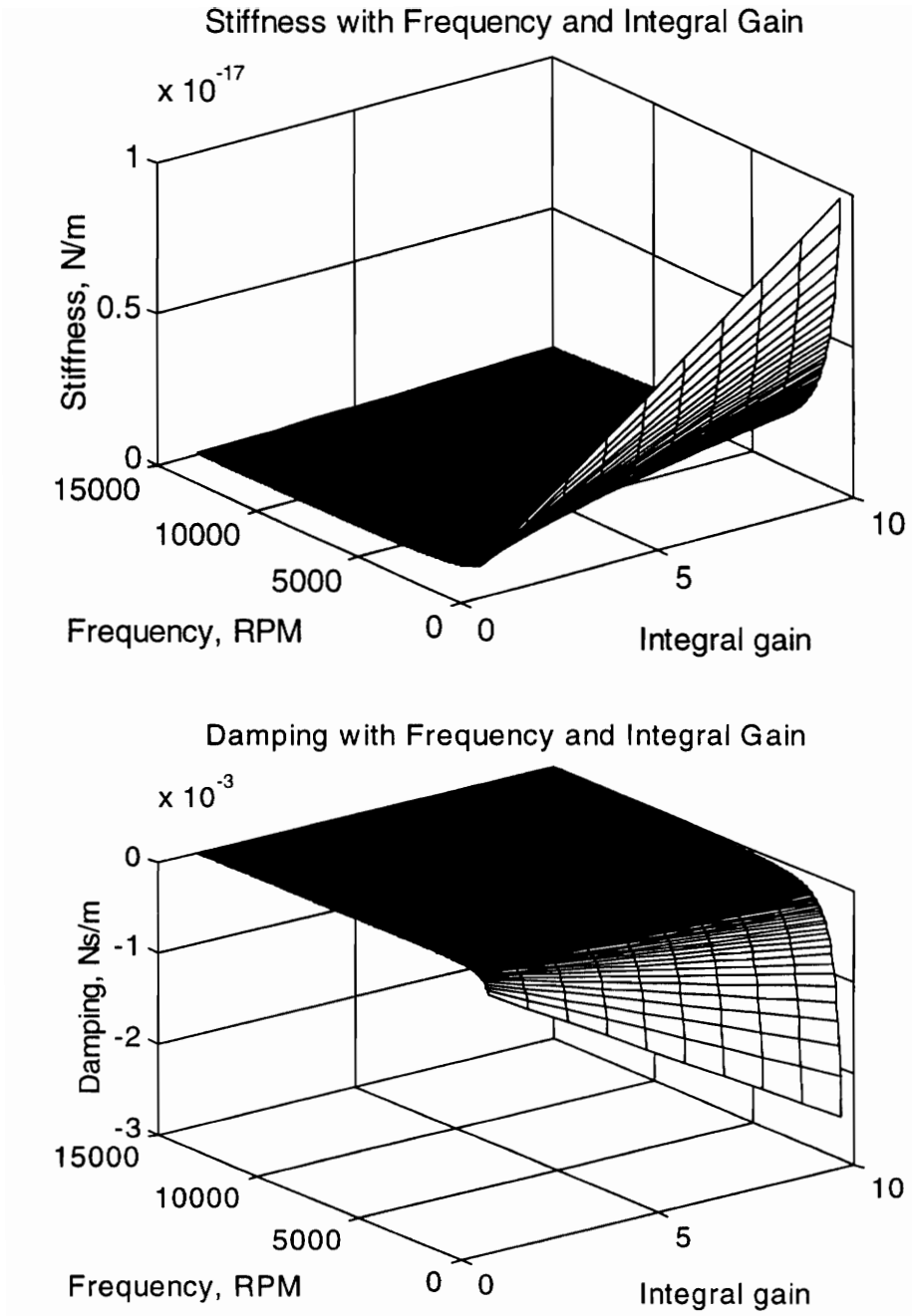

Figure 3.4: Variation of Stiffness and Damping with Integral Gain

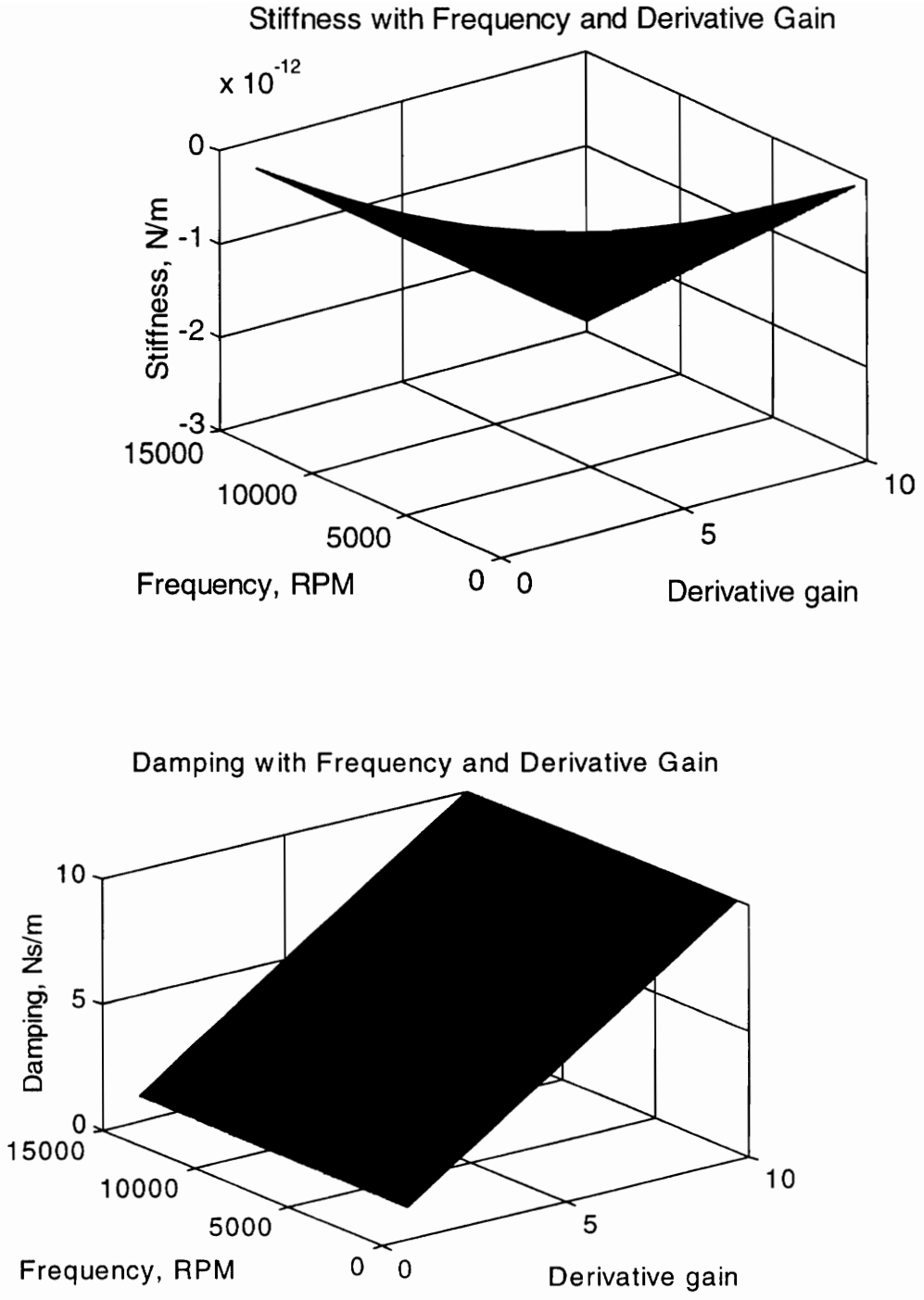

Figure 3.5: Variation of Stiffness and Damping with Derivative Gain

3.4 A Controlled Magnetic Bearing Supported Rotor

As discussed in Chapter 2, the rotor/bearing system consists of the rotor and the control system. In the previous sections we showed how to determine controller properties, and we presented a model of the rotor. Now we show how to combine the model of the rotor with the model of the control system transfer function for dynamic analysis.

Taking our finite element model of the rotor, with 'z' being the vector of coordinates ('x','y', 'Θ_x', and 'Θ_y') at each mass station, we include the forces due to the magnetic bearings and obtain:

$$[M][\ddot{z}]+[C][\dot{z}]+[K][z]=F_{ext}(t)+F_{mb}(t) \qquad (3.11)$$

where [M],[K],[C] are the mass, stiffness, and damping matrices, respectively. A small description of the coordinate system is shown in Fig. 3.6. At each mass element, four degrees of freedom exist. The first drawing shows a single rotor element and the translational coordinates at each. The second shows two rotor point masses and the angular coordinate between them. The angular coordinate in the direction perpendicular to the axis shown (i.e. the y-direction) is oriented in the same way.

$F_{ext}(t)$ contains the vector of external forces applied to the rotor/bearing system, typically in the form of an unbalance excitation. $F_{mb}(t)$ is a vector of magnetic bearing forces, and can be linearized and expanded to the following (similar to the magnetic suspension device):

$$F_{mb}(t) = -[k_i][i] - [k_z][z] \qquad (3.12)$$

These forces act at the bearing locations, stations 6 and 15 in the model. The free body diagrams in Fig 3.7 show the forces acting on the outboard end of the rotor, inboard end of the rotor, and the unbalance location (one of the disks, station 8,10 or 12). The matrices $[k_i]$ and $[k_z]$ are the magnetic bearing force-current matrix and the magnetic bearing nominal stiffness matrix, respectively. [i] is the vector of bearing currents (four total). (It is important to remember here that these currents represent the harmonic

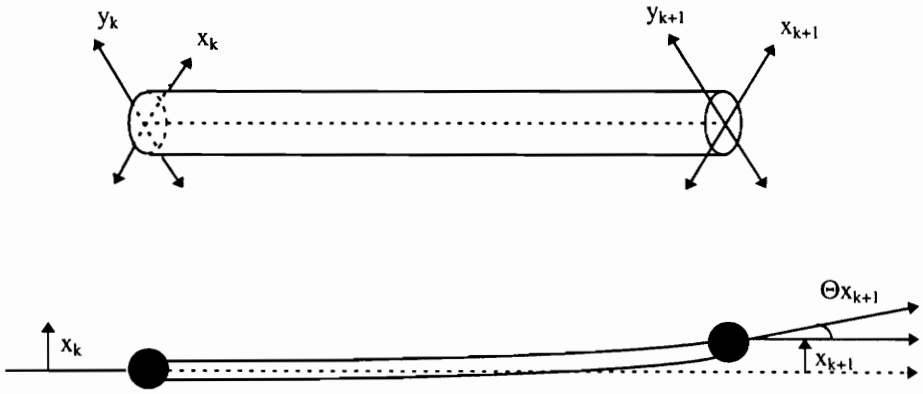

Figure 3.6: Coordinate System for the 3-disk rotor

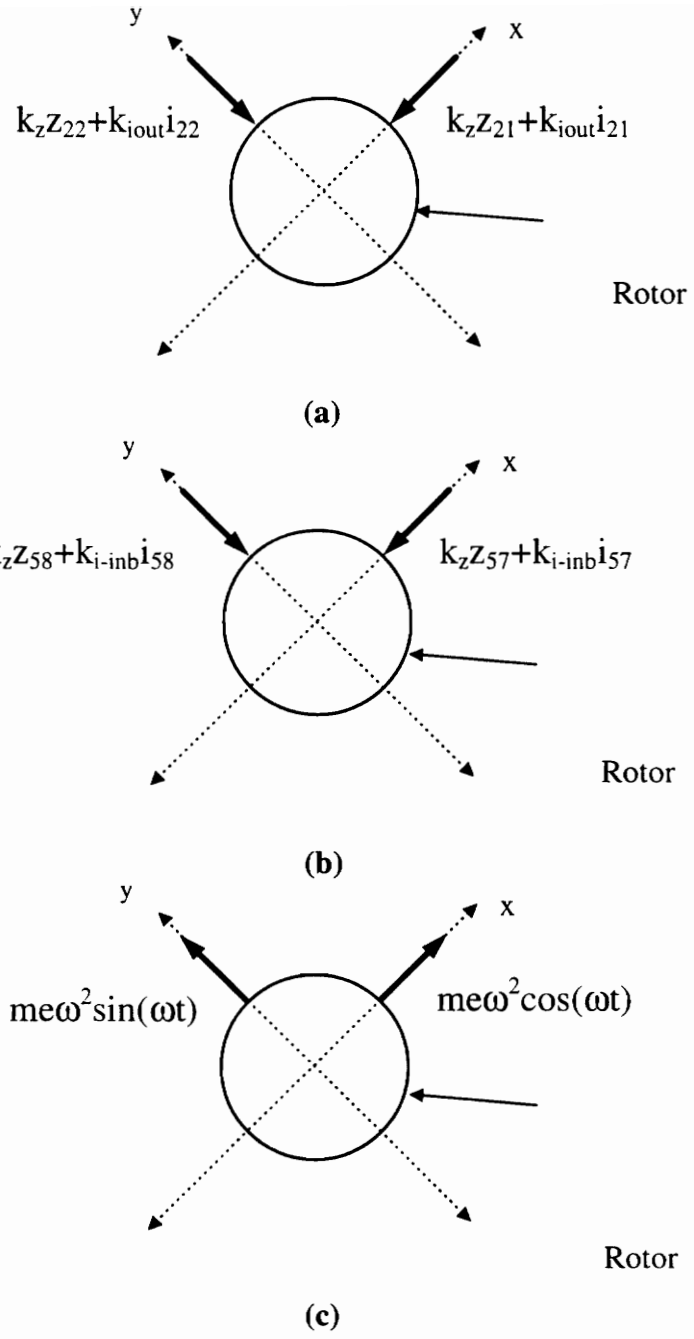

Figure 3.7: Free Body Diagrams showing forces acting on: (a) Outboard End of Rotor; (b) Inboard End of Rotor; (c) Unbalance Plane of Rotor

dynamic bearing currents supplied by the amplifiers rather than the bias current which supports the weight of the rotor at zero spin speed.) We looked at the force-current relationship in the previous chapter. The magnetic bearing nominal stiffness is also a function of bearing parameters such as bias current, projected area, number of coil turns, bias current, and nominal air gap. The equation for k_z, derived in Appendix A.1, is:

$$k_z = -\frac{2\mu_o A_g N^2 I_b{}^2}{G^3} \tag{3.13}$$

The bearing currents [I] are related to the displacements [Z] by:

$$[I(s)]=[G(s)][Z(s)] \tag{3.14}$$

where [G(s)] is a matrix of transfer functions relating each position sensed (four positions, the x and y at both bearing locations) to bearing current produced. The block diagram in Fig 3.8 shows the feedback paths and the formation of the control forces.

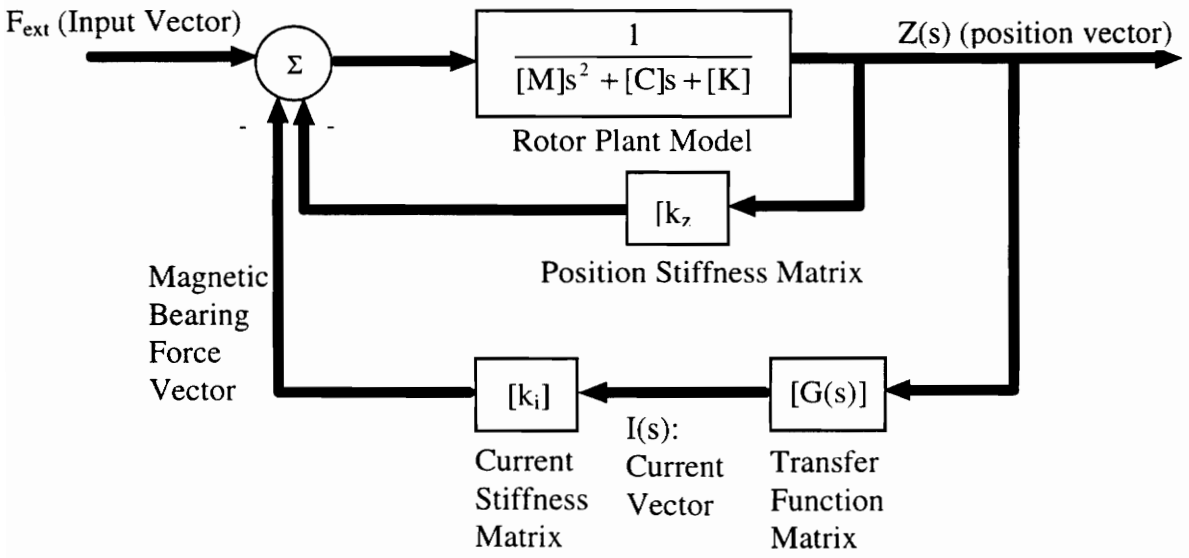

Figure 3.8: Block Diagram of Magnetic Bearing Controlled Rotor System

The transfer function matrix G(s) will be of dimension n x n, 'n' being the number of degrees of freedom in the model, but only four out of the n^2 entries in the matrix will be non-zero. Depending on whether or not collocation of bearings and sensors is assumed, the entries in G(s) will either be on the main diagonal or on the upper or lower diagonal. The model used in this thesis assumes collocated bearings and sensors. The actual bearings possess sensors located inboard of the bearings, as in Fig 3.9. The topic of collocation/non-collocation of sensors and bearings is now introduced in a small aside.

When the sensors and bearings are non-collocated, it means that along a control axis, the position feedback signal used by the control system to produce the bearing force is not the same coordinate as the one that the bearing acts upon. As in Fig 3.9 at the inboard bearing, the sensor senses coordinate x_{m+1} but the bearing force acts on coordinate x_m. The distance between the bearing and the sensor is small and the assumption that they deal with the same coordinate is usually adequate for lower rotor modes because the displacements are the same sense. As speeds increase and higher bending modes occur, the possibility of a node occurring between the bearing and sensor is real. If this occurs, the sensor will view a position of opposite sign than that at the bearing, and the force induced by the bearing will be the opposite of what is needed for stabilization, resulting in unstable vibration.

Returning to the expanded model, we see that the magnetic bearing force vector is now expressed entirely in terms of the displacement vector Z(s):

$$[M][Z(s)]s^2 + [C][Z(s)]s + [K][Z(s)] = [F_{ext}] - ([k_i][G(s)] + [k_z])[Z(s)] \qquad (3.15)$$

and we rearrange equation (3.15) to the following:

$$[M][Z(s)]s^2 + [C][Z(s)]s + [K + k_i G(s) + k_z][Z(s)] = [F_{ext}] \quad . \tag{3.16}$$

It is evident that implementing feedback control to the rotor/bearing system will affect the dynamic properties of the bearings, and thus will have an effect on the rotor stability and response. To see how the dynamic properties are affected, we can take the frequency

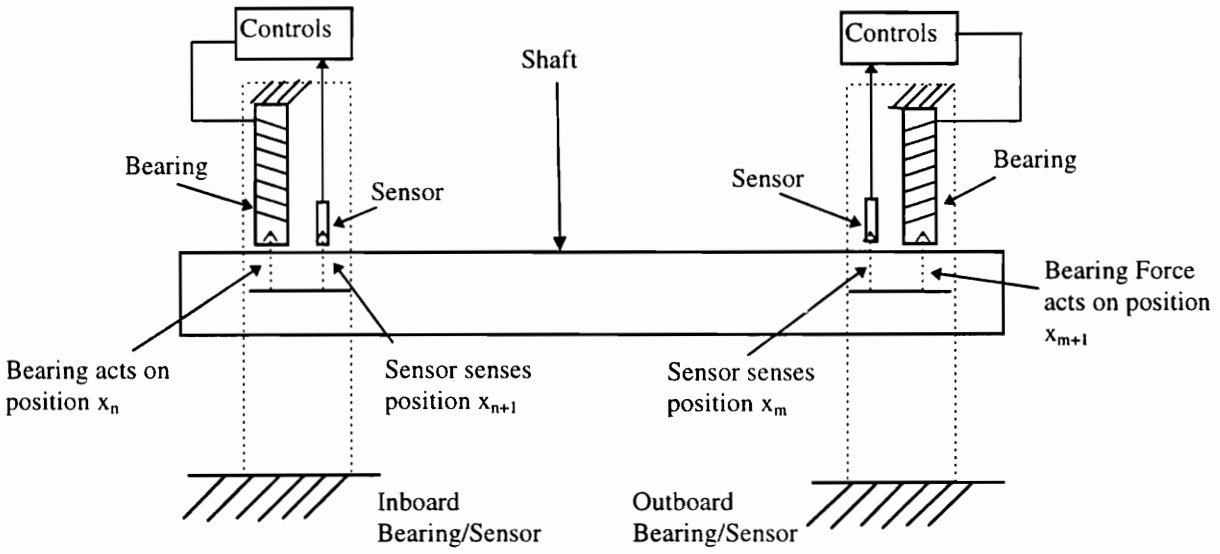

Figure 3.9: Sensor/Actuator Configuration in Test Rig

response of the system with respect to an unbalance excitation, where we assume circular synchronous response of the rotor:

$$-\omega^2[M][Z] + j\omega[C][Z] + [K + k_i G(j\omega) + k_z][Z] = [F_{ext}(j\omega)] \tag{3.17}$$

We can separate G(jω) into its real and imaginary parts, allowing the imaginary part to be included with the damping term:

$$-\omega^2[M][Z] + i(\omega[C] + k_i\ \mathrm{Im}(G(j\omega))[Z] + [K + k_i\ \mathrm{Re}(G(j\omega)) + k_z][Z] = [F_{ext}] \quad (3.18)$$

Looking at this formulation, it is evident that the "effective damping" matrix is composed of the original damping matrix [C] and a "dynamic" damping matrix due to the control system, and that the "effective stiffness" matrix is composed of the original stiffness [K], the magnetic bearing nominal stiffness matrix, and the "dynamic" stiffness matrix due to the control system:

$$[C_{eq}] = \frac{[k_i]\mathrm{Im}([G(j\omega)])}{\omega} \quad (3.19)$$

$$[K_{eq}] = [k_i]\mathrm{Re}([G(j\omega)]) + [k_z] \quad (3.20)$$

$$[C_{eff}] = [C] + [C_{eq}] \quad (3.21)$$

$$[K_{eff}] = [K] + [K_{eq}] \quad (3.22)$$

We must note that since each axis of control is independent of the others, the properties of each bearing axis is independent of the other axes as well, and since we assumed collocation, the bearing stiffness and damping matrices are diagonal. The locations of the entries on the diagonal matrices depend on the locations of the bearings. In the model used, the bearings are located at nodes 6 and 15. The x and y coordinates at station 6 are coordinates z_{21} and z_{22} and the x and y coordinates at station 15 are coordinates z_{57} and z_{58}. So the (21,21),(22,22), (57,57), and (58,58) locations in the stiffness and damping matrices of the bearings are the only ones populated.

Using the original mass matrix and the modified damping and stiffness matrices, we can form a new finite element model and solve for the forced response or stability at the bearing location (or anywhere else along the rotor), at the desired frequency, using the following equation:

$$[M][\ddot{z}]+[C_{eff}][\dot{z}]+[K_{eff}][z]=F_{ext}(t) \tag{3.23}$$

We have shown that the properties of the magnetic bearings are frequency dependent, so to solve for the forced response of the rotor across a range of frequencies, we need to change the values of the equivalent matrices of stiffness and damping at each desired frequency to the appropriate values based on the transfer function.

Revisiting the PID (Proportional-Integral-Derivative) compensator, it is useful to examine the equivalent bearing property matrices that are produced by this controller. We can look at the frequency response of the PID transfer function, as follows:

$$G_c(j\omega) = K_p + (K_d\omega - \frac{K_i}{\omega})j \tag{3.24}$$

Then, inspecting the real and imaginary parts separately, and accounting for the force/current stiffness, we can analytically evaluate the amount of stiffness and damping this controller generates for the magnetic bearing (assuming that each bearing axis is controlled identically and that we have four bearing axes of control):

$$[K_{eq}]=k_i\,\mathrm{Re}([G(j\omega)])=k_i[K_p] \tag{3.25}$$

$$[C_{eq}] = \frac{k_i\,\mathrm{Im}([G(j\omega)])}{\omega} = \frac{k_i}{\omega}([K_d]\omega - \frac{[K_i]}{\omega}), \tag{3.26}$$

which gives the following representations for the effective stiffness and damping:

$$[K_{eff}] = [K] + [k_i][K_p] \tag{3.27}$$

$$[[C_{eff}] = [C] + \frac{[k_i]}{\omega}([K_d] - \frac{[K_i]}{\omega}) \tag{3.28}$$

The plots earlier in this chapter show the variation of stiffness and damping with each PID parameter and frequency.

3.5 Current Control System

The control system in the control cabinet at the Rotor Dynamics Laboratory possesses a transfer function which has all the components in the feedback loop, as seen in the previous chapter. The previous sections have shown the effects that an ideal PID controller has on the bearing properties. Our control system is similar but not quite the same. It is therefore useful to examine the frequency dependent characteristics of the actual control system in the control cabinet to obtain an understanding of how the system's parameters affect the bearing properties.

Referring back to Figs 2.8 and 2.10, which show the entire control loop (Fig. 2.8) and the expanded view of the DSP portion of the control loop (Fig. 2.10), it is important to remember that the transfer function of the control loop must include all the different blocks present to obtain the correct bearing properties. Accordingly, the transfer function used to calculate the frequency dependent bearing properties (accounting for the different force-current relations at the inboard and outboard bearings) will be denoted G(s):

$$G(s)_{outboard} = k_{i_{outboard}} G_{cs}(s)$$
$$G(s)_{inboard} = k_{i_{inboard}} G_{cs}(s) \quad (3.29)$$

The portion of these transfer functions that we can control is the DSP board transfer function, or $G_c(s)$ as denoted in the previous chapter. The program which S2M provides to tune the control system presents the operator with several different parameters to change. These are summarized in the table below:

Table 3.1: Parameters in S2M Control System

Parameter	Current Setting
Proportional Gain (Kp)	1.25
Integral Gain (IG)	10
Integrator Cutoff Frequency (FCI)	2.00 Hz
Phase Lead #1 Angle, ϕ1	30 degrees
Phase Lead #1 Frequency	40 Hz
Phase Lead #2, Angle, ϕ2	30 degrees
Phase Lead #2, Frequency	500 Hz
Bandwidth Filter Damping	0.3
Bandwidth Filter Frequency	2400 Hz
Notch Filter #1, Gain	30
Notch Filter #1, Frequency	0 Hz
Notch Filter #2, Gain	30
Notch Filter #2, Frequency	0 Hz
Phase Bump Damping	0.3
Phase Bump Gain	1.3
Phase Bump Frequency	550 Hz

The integrator implemented in the control system is actually a first order system with a cutoff frequency at 2 Hz. From these parameters, the program calculates the transfer function coefficients shown in the previous chapter, and downloads these to the DSP boards. We must note again that since all four radial bearing control axes are tuned identically, the above parameters apply to all four radial bearing axes of control.

3.6 Dynamic Properties of The Current Control System

The program which S2M provides to tune the control system on the DSP boards in the control cabinet also has the ability to produce the bode plot (magnitude and phase) of the control system transfer function. It is useful to look at the variation in properties with frequency of this current controller setting, and also to confirm the transfer function through experiments.

To investigate the stiffness and damping of the control system as a function of frequency, we can generate the magnitude and phase data from the program and compute the real part (which corresponds to the stiffness) and the imaginary part divided by the frequency (which corresponds to the damping). The resulting units are not in the standard form for stiffness and damping because we are only considering the control system portion of the control loop, as opposed to the entire loop which includes the sensors, amplifiers, and the magnetic bearings. However, since we represent these other parts of the control loop as DC gains, the stiffness and damping curves for the entire control loop are just

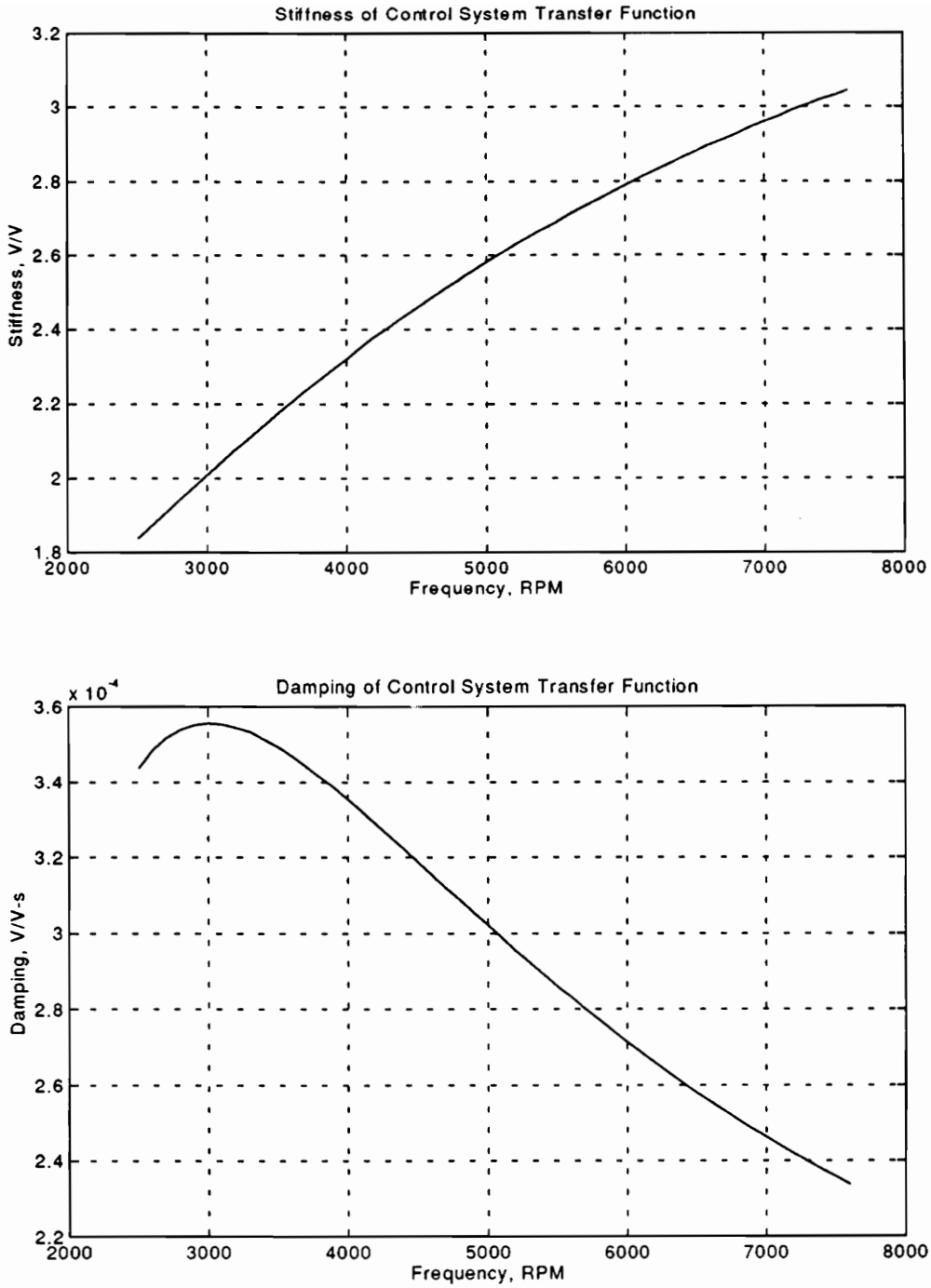

Figure 3.10: Stiffness and Damping of Control System with Current Settings

multiples of the plots shown for the control system. Figure 3.10 shows the variation of "stiffness" and "damping" of the control loop with frequency at the settings in table 3.1. The stiffness increases steadily with frequency up to the running speed of 8000 RPM, while the damping increases up to a point around 3000 RPM at which point it drops off again at a steady rate.

The above plots represent how the magnetic bearing properties will vary with frequency of vibration of the rotor (with the other gains factored in). Variation of the parameters in the control system will obviously affect these properties. The following chapter will describe how the variation of parameters affects the properties and how these changes in properties affect the rotor/bearing system. It will also describe the experiments performed to view the effects of these changes.

3.7 A Design Procedure and Example

In this chapter we have seen how to determine a control system's effective properties and how these effective properties can be implemented into the plant model for dynamic analysis. This method can also be considered a design tool for the design of a control system. For example, if we want to produce a certain shift in the system's natural frequency, we can change the stiffness of the system by careful design of the control system transfer function. If the system is designed to oscillate at certain frequencies, we place the natural frequencies away from these design frequencies. Similarly, if we want a certain peak vibration level and peak vibration frequency, we can change the system's

damping through control system design. To avoid large amplitudes of response at natural frequencies, the damping of natural modes can be adjusted to flatten out peak response levels. These broad statements can also be applied to rotor/bearing systems. It has been shown that the critical speeds of rotors are greatly dependent upon the stiffness of the bearings supporting the rotor. Also, the peak vibration level at critical speeds depends on the damping of the bearings. Since with magnetic bearings, the damping and stiffness are dependent upon the design of the control system, the designer can choose desired response characteristics and design the control system to produce these characteristics.

With these thoughts in mind, it is useful to demonstrate the design of a control system for the magnetic suspension device in chapter 2. This system is greatly similar to the behavior of magnetic bearings and the design procedure here can be expanded and applied to the individual magnetic bearing control systems. Revisiting the block diagram of the closed loop magnet/ball suspension system with the current in the magnet a function of the magnet's displacement:

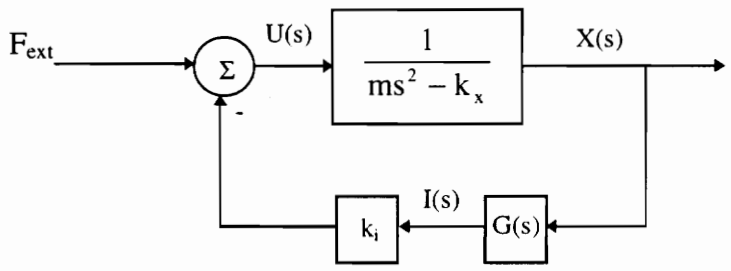

Figure 3.11: Closed Loop Block Diagram of Controlled Suspension Device

we see that the open loop transfer function of the system is unstable. However, we can design the feedback transfer function G(s) to stabilize the system. Writing an expression for the control input U(s) in terms of the position output X(s), we get

$$U(s)=F_{ext}-k_i G(s)X(s) \tag{3.30}$$

and since we know

$$U(s)=(ms^2-k_x)X(s) \tag{3.31}$$

we can form the closed loop transfer function for the output X(s) and the input F_{ext}.

$$\frac{X}{F_{ext}}=\frac{1}{ms^2-k_x+k_i G(s)} \tag{3.32}$$

At this point we will assign numbers to the system.

Table 3.2: Suspension System Example: Numeric Values

Parameter	Value
Ball Mass	0.25 kg
Magnet Nominal Stiffness	5 N/m
Force-current Relation	2 N/A

System Stabilization

To first stabilize the system, we must make sure that the magnitude of the stiffness added to the system by the transfer function is greater than that of the stiffness of the magnet. To stabilize the system, the following relation must be true:

$$k_{eq} = k_i \, \mathrm{Re}(G(s)) - k_x > 0 \tag{3.33}$$

or :
$$\mathrm{Re}(G(s)) > \frac{k_x}{k_i} = \frac{5}{2} = 2.5 \tag{3.34}$$

Changing the Natural Frequency

Let's say for a design goal, we want to place the natural frequency of the system at 2 rad/s. This gives us a required k_{eq} value of:

$$k_{eq} = \omega^2_n m = 4(0.25) = 1 \tag{3.35}$$

and thus:
$$\mathrm{Re}(G(s)) = \frac{k_{eq} + k_x}{k_i} = \frac{1+5}{2} = 3, \text{ or } G(s) = 3. \tag{3.36}$$

With this transfer function implemented, the system is stabilized but without damping, an excitation at this natural frequency will result in an unstable response. The system's eigenvalues are $\pm 2i$.

Changing Peak Amplitude

We need to add some damping to the system to keep response amplitudes at reasonable levels. Let's say we want to have a peak magnification factor equal to four. Using theory, this means that we want a damping ratio of:

$$\zeta=\frac{1}{2Q}=\frac{1}{2(4)}=0.125 \tag{3.37}$$

and $$c = 2m\omega_n\zeta = 2(0.25)(2)(0.125) = 0.125 \tag{3.38}$$

We know that the damping of the system is:

$$c=k_i\frac{\mathrm{Im}(G(j\omega))}{\omega} \tag{3.39}$$

If we implement a differentiator, whose transfer function is $G(s)=K_d s$, the damping value becomes dependent on K_d alone: $c = k_i K_d$.

Thus we can calculate the value of K_d required to produce the magnification level:

$$K_d = \frac{c}{k_i} = \frac{0.125}{2} = 0.0625 \tag{3.40}$$

We can alter the system damping by altering the derivative gain of the transfer function. The new eigenvalues are now $-0.25 \pm 1.9843i$, which possess the desired damping ratio and natural frequency. The peak magnification factor is now equal to four, whereas before it was infinite without damping.

Design Summary

The overall transfer function designed is $G(s)=0.0625s + 3$. This transfer function accomplishes three tasks: it stabilizes the system, it shifts the natural frequency to a

desired location, and it adds damping to reduce peak amplitudes. Making the analogy to magnetic bearings, the first goal is the same, to stabilize the system. The second goal, to move the natural frequency, is equivalent to shifting the critical speed(s) of the rotor. The third goal, adding damping to reduce peak amplitudes at critical speed, is a common goal for machine performance.

3.8 Chapter Summary

This chapter began by reiterating the requirement of active feedback control for stabilization of magnetic bearings, and showed how to determine a control system's effects on a plant's dynamic properties. We then demonstrated the effects of the gains of a PID controller on dynamic properties. We showed to combine the rotor model and the control system controlling the magnetic bearing forces, for stability and response. We showed the properties of the control system presently in the laboratory, including the tuning parameters present. Finally, we showed a design procedure and an example for the control system for the magnetic suspension device introduced in chapter 2, and made the analogy between this system and a magnetic bearing supported rotor to show that the basic design technique is the same.

Chapter 4 describes the experiments and simulations performed to view the effects of control system parameter variation, and the experiments performed to identify the characteristics of the control system.

Chapter 4: Experiment and Simulation Description

In this chapter, we describe the experiments performed with the magnetic bearing supported 3-disk rotor test rig, and the simulations performed as a measure of comparison to the experimental data. This chapter begins with an explanation of the forces exerted by a mass unbalance on a spinning rotor, then describes the experiments performed to accomplish various tasks with the test rig. We show a table of the first two modes of the supported rotor as functions of spin speed, to get an idea of the location of peak response speeds. We then show the procedure used for simulation of the magnetic bearing supported rotor with a mass unbalance attached, and provide a segue to the next chapter.

4.1 Rotating Unbalance: Theory

It is well known that if a known mass 'm' is allowed to rotate about the center of rotation of a system at an eccentricity 'e', the force that this mass exerts on the system is a function of the mass 'm', the eccentricity 'e', and the frequency of rotation 'ω' (expressed in complex notation):

$$F_{unbalance} = me\omega^2 \cdot e^{i\omega t} \tag{4.1}$$

Figure 4.1 shows a single degree of freedom system excited by a rotating unbalance and a free body diagram showing the forces acting on the system

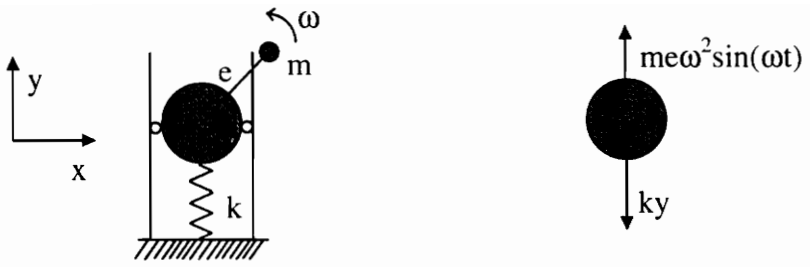

Figure 4.1: Rotating Unbalance Excitation and Free Body Diagram

Considering our 3-disk rotor, if we attach a known mass unbalance to one of the disks on the rotor, the forces exerted on the rotor at this location along the rotor's x and y axes are (as seen in Fig. 3.6):

$$\begin{Bmatrix} F_x \\ F_y \end{Bmatrix} = \begin{Bmatrix} me\omega^2 \cos\omega t \\ me\omega^2 \sin\omega t \end{Bmatrix} \tag{4.2}$$

where 'ω' is the frequency of rotation of the rotor, which is equivalent to the running speed of the rotor. So if we are running the rotor at a speed of 6000 RPM (revolutions per minute) then the frequency of excitation 'ω' is equivalent to the running speed. Also, the frequency of whirl of the rotor in response to an unbalance excitation is equivalent to the frequency of excitation, which is equivalent to the running speed.

4.2 Experiments

The experiments were conducted on the magnetic bearing test rig described in earlier chapters. The goal of the first set of experiments was to determine the characteristics of the control system DSP board. Using the information gathered in this

first set of experiments, the second set of experiments obtains forced response data for the rotor with the nominal control system settings, to compare to the simulated forced response for model verification. The third set of experiments consists of parameter variation in the control system and viewing the effects that these variations have on the forced response characteristics.

4.2.1 System Identification Experiments

It is important to know the true characteristics of the entire control loop, because the control system transfer function is what determines the magnetic bearing properties as a function of frequency. Therefore, to ensure that we are representing the characteristics of the bearings accurately, we can perform testing to determine the true characteristics of several portions of the control loop. The block diagram in Fig. 4.2 shows the portions of the loop which were identified:

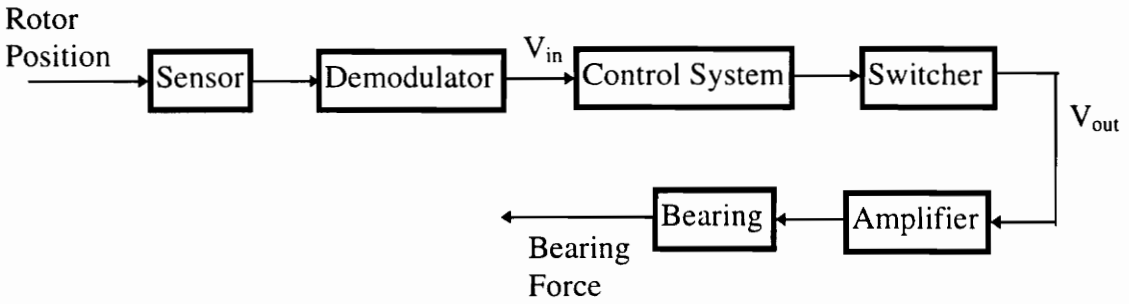

Figure 4.2: Block Diagram Showing Measured Portions of Control Loop

The control cabinet allows the viewing of the signal at the output of the demodulator, labeled V_{in}, the amplifier command voltage, V_{out}, and the current generated in the bearings, i_c.

If we run the rotor at a constant speed, then the whirl frequency of the rotor is equivalent to this constant speed assuming 1X synchronous response. Therefore the signal V_{in} is a harmonic signal with frequency equal to the running speed. The amplifier command voltage and the current supplied to the bearings are harmonic signals of the same frequency. The following steps detail the procedure followed to obtain the frequency response of the control system in the cabinet.

1. Perform all the necessary pre-startup checks and steps for the magnetic bearing test rig.
2. Start the shaft rotating and adjust the speed control until the speed is 2000 RPM.
3. Hook up Channel 2 of the Tektronix Fourier analyzer to the amplifier command signal for the V13 axis amplifier in the cabinet.
4. Hook up Channel 1 of the analyzer to the demodulator output signal in the V13 axis in the cabinet.
5. Make sure the signals are the expected harmonics by looking at instantaneous time histories of both. Also look at the autospectrum of both to ensure that the frequency content of both is predominantly at the running speed frequency.
6. Set up the analyzer for time averaging with 50 averages.

7. Run the XFER function on the analyzer with Channel 1 as the input and Channel 2 as the output.

8. When the averaging is complete, record the magnitude relationship and the phase relationship of the Channel 2 / Channel 1.

9. Repeat steps 3 through 8 for the the W13, V24, and W24 bearing axes. .

10. When all four control axes have been measured and recorded, increment the speed by 100 RPM with the speed control and repeat steps 3 through 9.

We obtained data from 2000 RPM to 8000 RPM in 100 RPM increments for all four control axes, magnitude ratio and phase angle. The results of these experiments are shown in the next chapter.

4.2.2 Model Verification

Using the knowledge gained from the system identification experiments performed, the next step is to run a forced response of the rotor with a known unbalance attached to one of the disks. Since this forced response is a frequency response of the rotor with respect to the rotating unbalance input, we can use the response for model verification of the rotor/bearing system by comparing simulation results to the experimental forced response results obtained here. The steps followed to obtain the forced response of the rotor to a known unbalance input were as follows:

1. Perform all the necessary pre-startup checks and steps for the magnetic bearing test rig.

2. Do not attach the unbalance weight yet.

3. Start the shaft rotating at 2000 RPM using the speed control.

4. Prepare the Bently-Nevada data acquisition system (Bently box) to acquire runup data every 50 RPM increasing. The system acquires data in the form of magnitude of the position sensor signals (in volts) and phase angle of the sensor signal with respect to the keyphasor, for each position sensor, in all four radial bearing axes.

5. By hand, slowly start to increase the speed of the rotor. If this is done too quickly, the Bently box cannot sample quickly enough and inaccurate data results.

6. Slowly increase the speed of the rotor up to 8000 RPM. The Bently box should flash each time it acquires data every 50 RPM.

7. When the speed reaches 8000 RPM, hit the stop button on the motor controller box. Using the accompanying computer, run the ADRE program and download the just-obtained data from the data acquisition system. Save the data, and print out the tabular response for the V13, W13, V24, and W24 bearing axes.

8. This response is the balance condition for the rotor.

9. Attach the known unbalance weight to the outboard disk in the rotor and repeat steps 3-7. This response is the forced response of the rotor due to the unbalance input.

The balance condition is the response of the rotor with respect to its inherent unbalance. Once the balance condition is obtained for the four probes of interest, we can

run a forced response test with a known unbalance mass and measure the response in the same way as the balance condition. It is important to measure the mass and the eccentricity of the unbalance, and then to note the disk in which the mass is placed. For this verification experiment, the unbalance mass was placed in the outboard disk with the control system at the nominal settings. Table 4.1 gives the pertinent data for the forced response test.

Table 4.1: Forced Response Test Data

Unbalance Mass: 0.2735 oz	**Eccentricity: 4 in**

In SI units, the mass-eccentricity value (mass multiplied by eccentricity) is 7.268 x 10^{-4} kg-m. The forced response data is acquired in the same way as the balance condition data for each radial bearing sensor.

By the principle of superposition, the response of the rotor when excited by a known rotating unbalance mass is a combination of the response to this mass unbalance force and the response to the inherent unbalance in the rotor. Let's say that at one frequency and one bearing axis the balance condition response amplitude is 0.10 mils (thousandths of an inch) peak to peak at a phase angle of 290 degrees with respect to the keyphasor, and the forced response amplitude is 1.00 mils peak to peak at a phase angle of 320 degrees. Then to find the response due to just the mass unbalance, we can vectorially subtract the balance condition response from the forced response.

$$R_{net} = 1\angle 320 - 0.10\angle 290 = 0.915\angle 323 . \qquad (4.3)$$

The net response is 0.915 mils at a phase angle of 323 degrees. While this is not a large deviation from the original forced response, it is significant enough to make a difference in comparisons to simulations, which will produce the response for a "perfectly balanced rotor".

The procedure in the section above is performed for the tabular data for all four radial bearing axes across the range of frequencies to obtain the response which would be obtained from a "perfectly balanced" rotor. This involved 61 vectorial subtractions for each of the four bearing axis. The resulting response data is used for comparison to the simulated responses to check the accuracy of the model.

4.2.3 Parameter Variation Experimentation

Once the forced response is obtained for the nominal control system settings to check the veracity of the model, the next step is to vary parameters in the control system and view the effects on the forced response of the rotor.

As seen in the previous chapter, the control system allows several different parameters to be tuned. We will focus on two: the proportional gain and the integral gain. The analysis of the effects of changing these parameters is straightforward (just altering the bearing properties based on the change) and previous works (Williams et. al) have performed experiments varying similar parameters in the control system. This allows comparison of the results obtained in this work to those obtained in previous work.

From the nominal setting of the control system, we tune the control system to the settings in Table 4.2, obtain the balance condition, then obtain the forced response with a known unbalance in the outboard disk and perform the vectorial subtraction to obtain the response for a "perfectly balanced" rotor. The steps taken for these experiments are identical to those undertaken for the model verification experiments.

Table 4.2: Controller Settings for Experimentation

Setting #	Proportional Gain	Integral Gain
1	1.25	10
2	0.85	10
3	1.7	10
4	0.85	5

The results of these experiments are presented in the next chapter.

4.3 System Simulation with Matlab

4.3.1 System Model

In the previous chapter, we showed how to obtain a finite element model of the rotor/bearing system by using the magnetic bearings' frequency dependent properties in conjunction with the rotor matrices. Since the bearing properties are frequency dependent, the effective stiffness and damping matrices will change with whirl frequency or running speed. The equations which govern the behavior of the rotor/bearing system at a single frequency of excitation is:

$$[M][\ddot{z}] + [C_{eff}][\dot{z}] + [K_{eff}][z] = [F_{ext}] \tag{4.4}$$

The external force vector is composed of the unbalance forces due to the rotating unbalance. Depending on which disk the unbalance is attached to, the unbalance forces will be in different locations in the external force vector. For an example, if the unbalance is attached to the outboard disk, which corresponds to station number 8 in the rotor model, the unbalance force will excite the x and y coordinates at this station, which correspond to coordinates z_{29} and z_{30}. The unbalance force vector for this example is :

$$[F_{ext}] = \begin{bmatrix} 0 \\ \cdot \\ \cdot \\ F_{z_{29}} \\ F_{z_{30}} \\ \cdot \\ \cdot \\ 0 \end{bmatrix} = \begin{bmatrix} 0 \\ \cdot \\ \cdot \\ me\omega^2 \cos\omega t \\ me\omega^2 \sin\omega t \\ \cdot \\ \cdot \\ 0 \end{bmatrix}$$

A similar unbalance force vector is formed for an unbalance attached to the midspan disk, except the unbalance forces excite the coordinates at station number 10, z_{37} and z_{38}.

4.3.2 Calculating the Response

When we have the model of the rotor/bearing system at the individual frequency of interest and the correct input force vector, we can simulate the system as we would any other dynamic system. We must note again that since the bearing properties are dependent on frequency, the model matrices change at each frequency of simulation. We

form a state space representation of the system as follows and use the **lsim** command in Matlab to obtain the response.

$$A = \begin{bmatrix} 0 & I \\ -M^{-1}K_{eff} & -M^{-1}C_{eff} \end{bmatrix}, B = \begin{bmatrix} 0 \\ M^{-1} \end{bmatrix} \tag{4.5}$$

where the state vector is $w = \begin{bmatrix} z \\ \dot{z} \end{bmatrix}$, where z is the coordinate vector as defined in equation (2.7). The dimensions of the matrices are: A (160 x 160), B (160 x 80) The output matrix C (4 x 160) gives the x and y responses at the two magnetic bearing locations, and the feedthrough matrix D (4 x 80) is a matrix of zeros. The Matlab code generates this state space model for each frequency point and calculates the amplitude and phase lag for each bearing axis.

Using the Matlab code developed, we first simulated the system for the model verification conditions (nominal control system settings, unbalance in outboard disk). Then, for each controller setting and each unbalance location for which we performed parameter variation experiments, we simulated the same conditions using the technique in this section. The comparisons of these simulations to the experimental data are shown in the following chapter. The flowchart in Fig. 4.3 shows the procedure that the code undertakes to solve for the response.

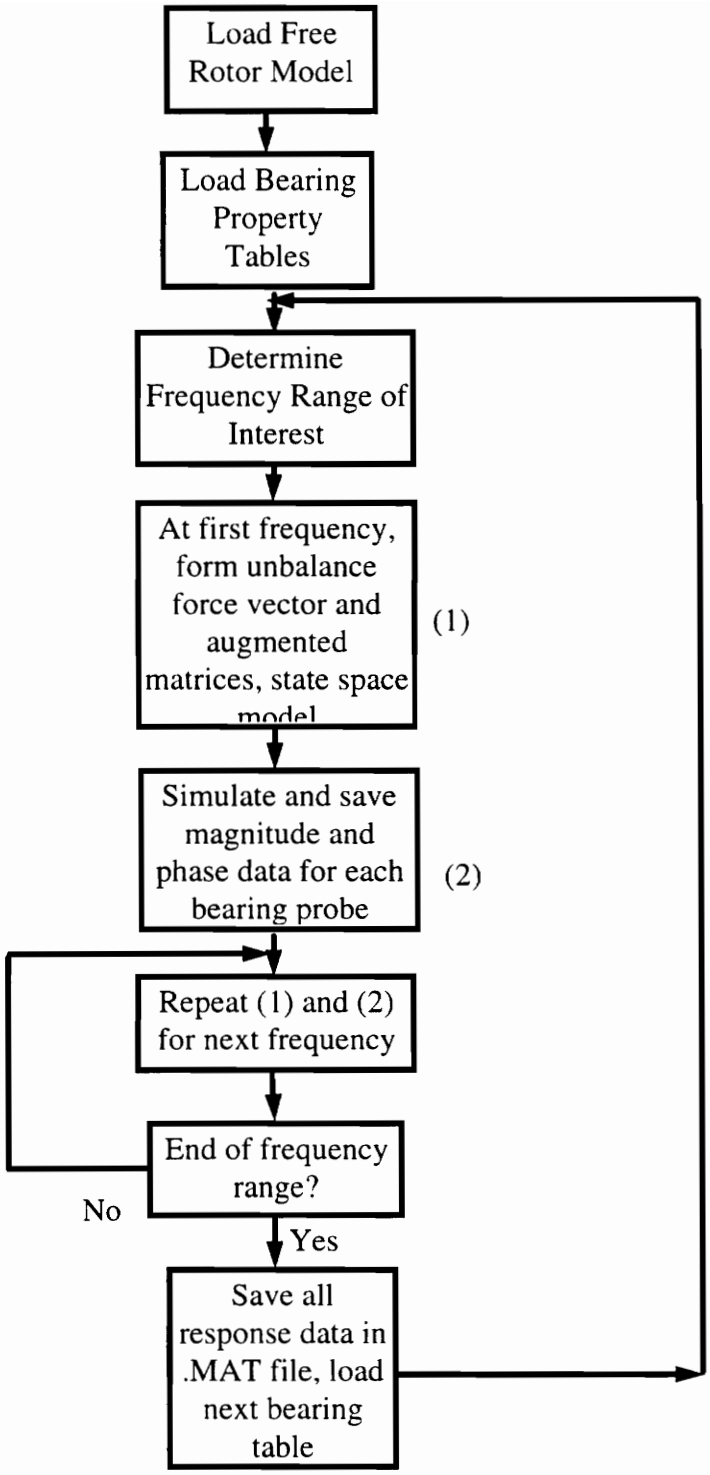

Figure 4.3: Flowchart of Matlab Simulation Procedure

4.4 Critical Speeds and Mode Locations

As the rotor spins at a given speed, the resulting whirl frequency will be predominantly the same as the spin speed. This means that the effective bearing properties will vary with spin speed, and thus the dynamics of the supported rotor change as well. Table 4.3 shows the variation in the first two forward and backward undamped whirling modes as functions of spin speed. To determine these frequencies, the bearing properties were taken at the nominal control system settings.

Table 4.3: First Two Rotor Modes Under Nominal Bearing Properties

Running Speed (RPM)	First Backward Mode (RPM)	First Forward Mode (RPM)	Second Backward Mode (RPM)	Second Forward Mode (RPM)
2000	3341.5	3341.6	3940.6	3940.6
3000	3656.5	3656.6	4320.6	4320.8
4000	3917.2	3917.3	4637.1	4637.4
5000	4117.1	4117.3	4881.3	4881.6
6000	4269.3	4269.5	5068.1	5068.4
7000	4387.6	4387.8	5213.8	5214.2
8000	4482.9	4483.1	5331.7	5332.1

While these values are only valid at the nominal control system settings, they do serve to give an idea of the natural frequencies as the rotor runs up to 8000 RPM. When the rotor speed and the natural frequencies that coincide to that rotor speed become the same, the speed is a critical speed.

4.4 Chapter Summary

This chapter has gone over the experiments and simulations performed. Experiments to identify and/or confirm several portions of the control loop were conducted, then we conducted a forced response test to verify the model of the rotor/bearing system, with the nominal as-tuned controller settings present in the control system. After these tests, we perform experiments varying control system parameters, to view the effects of these variations on the forced response characteristics of the rotor.

We performed simulations of the rotor/bearing system as a method of prediction of the forced response of the rotor. First, we simulate the system with the nominal control system settings and compare the response to the experimental data with these settings, for model verification. Then, we simulate the system varying the control system parameters and compare these results to the experiments.

The next chapter provides tabular and graphical interpretation of the experimental and simulation results obtained, and discusses the implications of these results.

Chapter 5: Results and Discussion

5.1 Control System Identification

In the previous chapter, we discussed the experimental method used to identify the characteristics of the DSP board portion of the control system transfer function. This section will present the results of these experiments. As stated earlier, the control system is tuned identically for each bearing radial axis of control. Thus, the frequency response of the control system transfer function should be the same for each control axis, all identical to the predicted transfer function from the S2M program.

Figure 5.1 shows the experimental data for the control axis V13 (the x-axis at the outboard bearing) compared to the theoretical data obtained from the program. Figure 5.2 shows the comparison for W13 (the y-axis at the outboard bearing). Figure 5.3 shows the comparison for V24 (x-axis at the inboard bearing). Finally, Fig. 5.4 shows the comparison for W24 (y-axis at the inboard bearing).

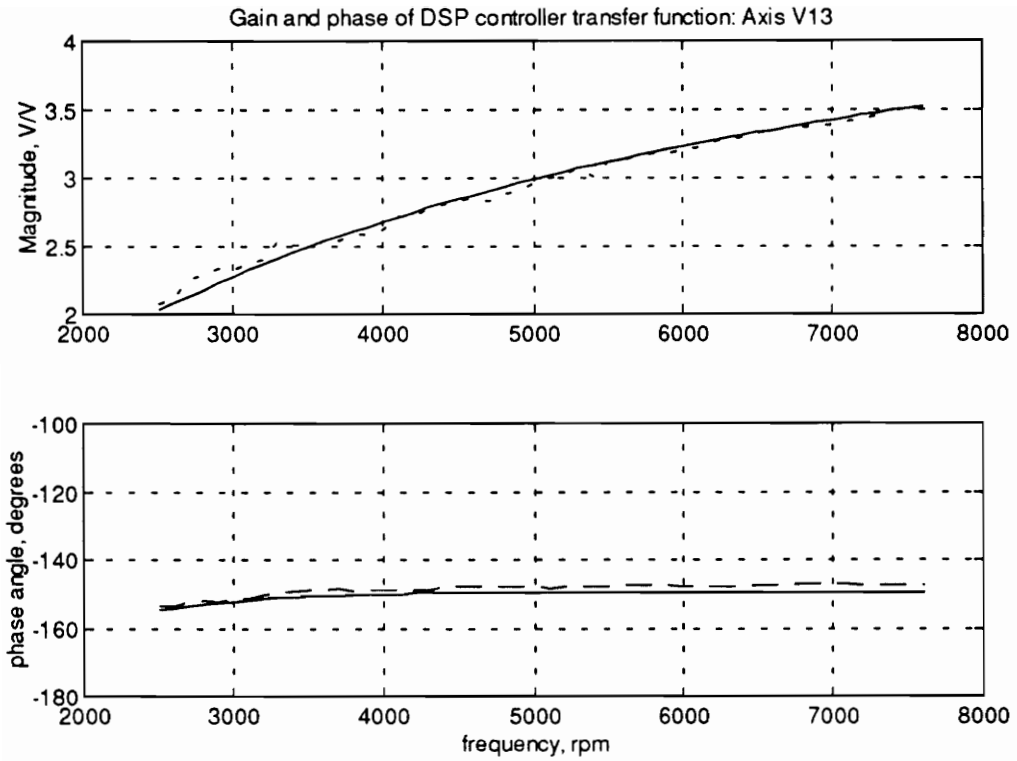

Figure 5.1: Axis V13 DSP transfer function

(solid = theoretical, dashed =experimental)

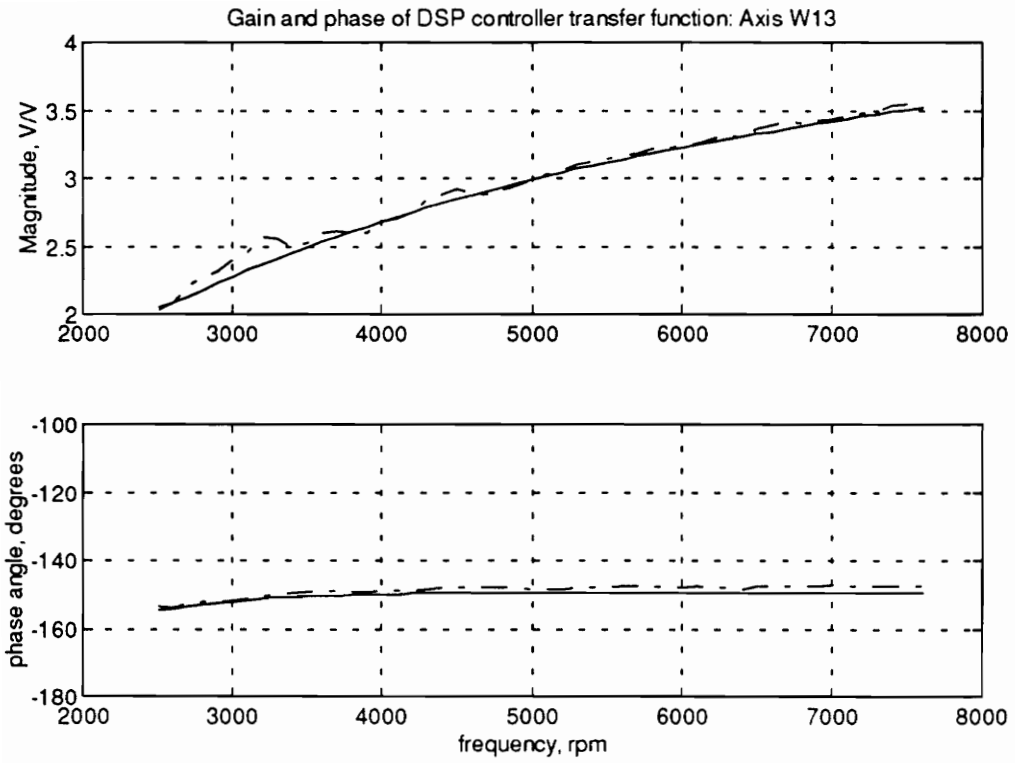

Figure 5.2: Axis W13 DSP transfer function

(solid=theoretical, dashed = experimental)

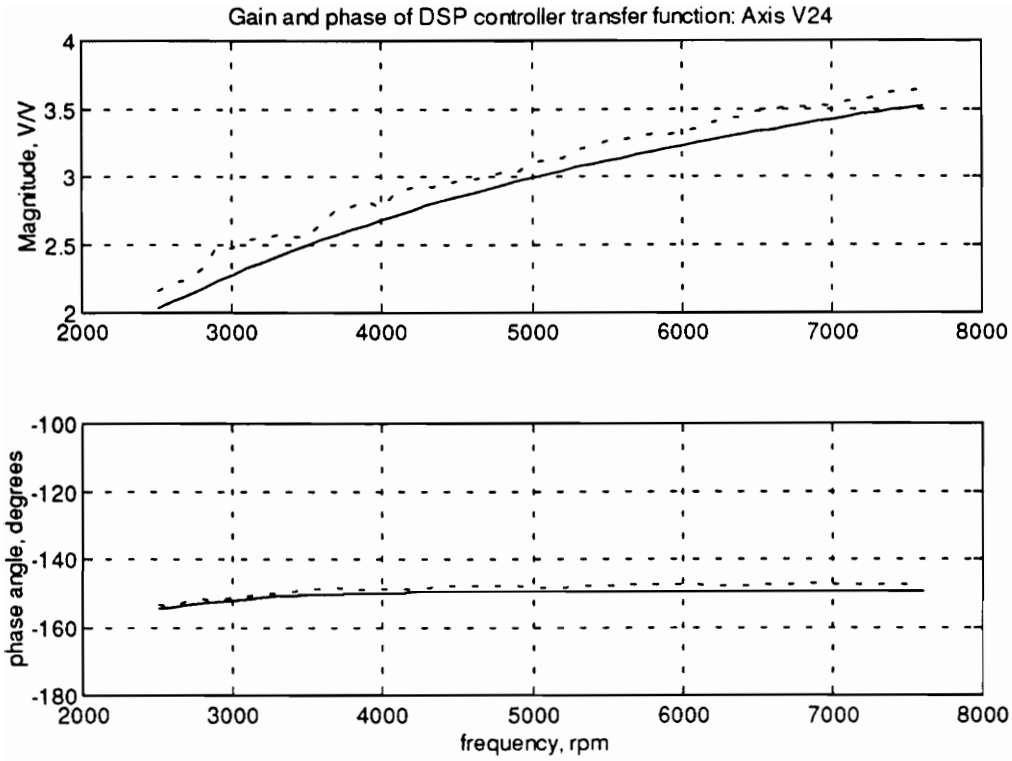

Figure 5.3: Axis V24 DSP transfer function

(solid = theoretical, dashed = experimental)

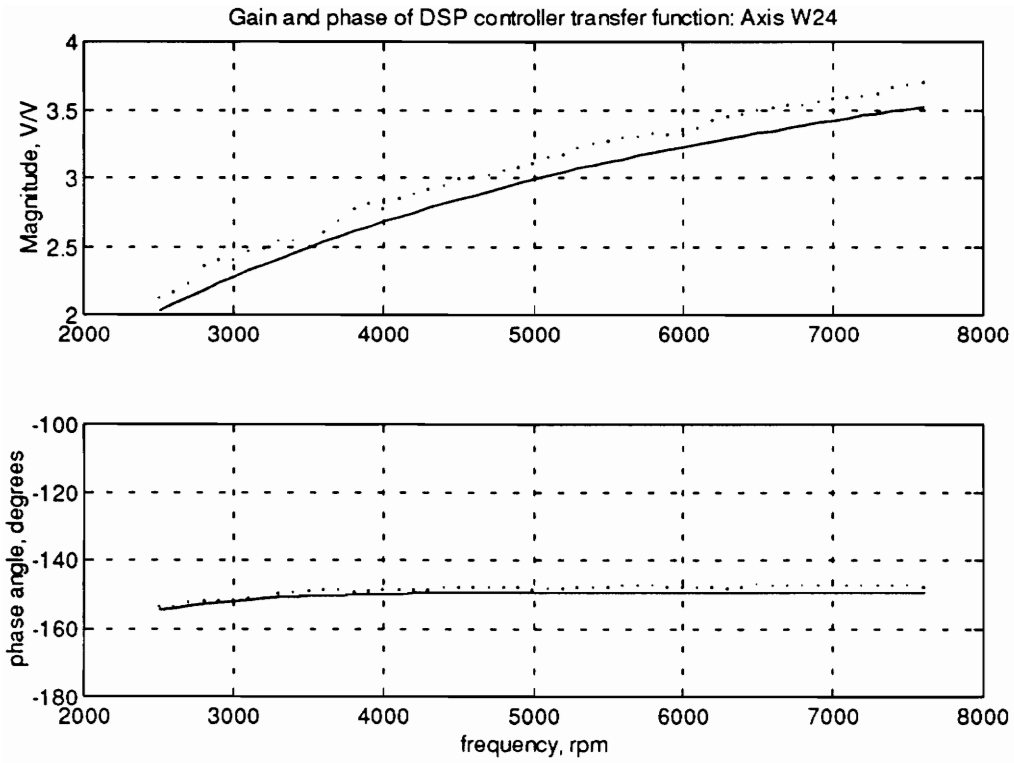

Figure 5.4: Axis W24 DSP transfer function

(solid=theoretical, dashed = experimental)

All four axes of control show excellent agreement with the theoretical prediction of gain and phase. The gain in axes V24 and W24 is slightly higher than the theoretical, whereas with V13 and W13, the gain is uniformly near the theoretical. Since the two bearings are controlled by separate DSP boards (one for the inboard, one for the outboard), this indicates that the inboard DSP board may be flawed slightly. The phase angles for all four transfer functions are similar and very close to the theoretical prediction. Overall, this experiment confirms the predictions of the program.

5.2 Results of Nominal Forced Response Experiments

As a check on the accuracy of the rotor/bearing system model developed in chapter 3, a forced response across the range of running speeds of the rotor was performed with a known unbalance mass in the outboard disk of the rotor, and the response measured at the four radial bearing axes. Using the balance condition data obtained prior to the forced response testing, the forced response of the rotor due to the unbalance alone was obtained. The control system settings for this testing were: Kp = 1.25, IG = 10.

Because the frequency dependent bearing properties determine the location and levels of peak responses, we show them here. Figure 5.5a shows the inboard and outboard bearing stiffnesses with frequency, and Fig. 5.5b shows the inboard and outboard bearing damping with frequency.

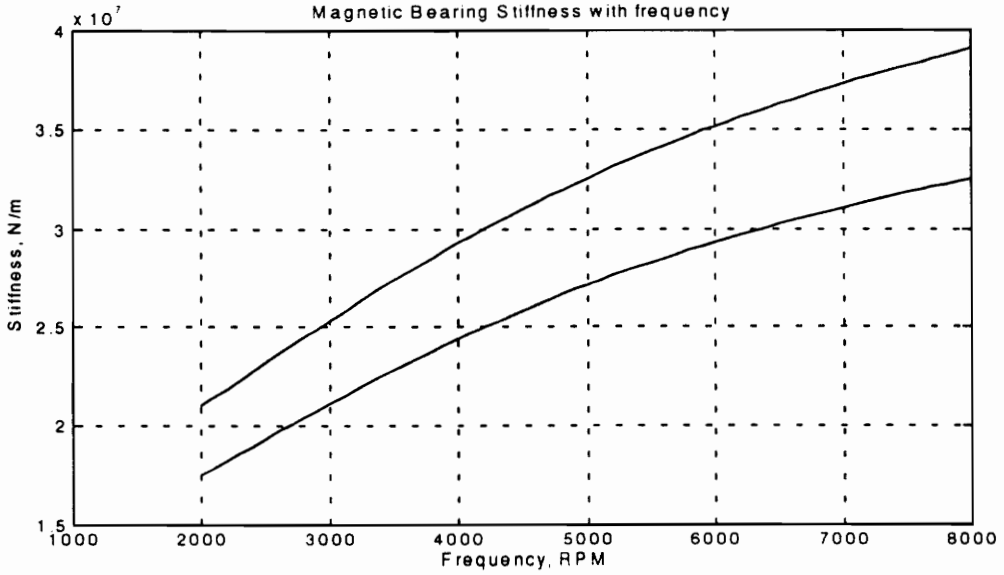

(a)

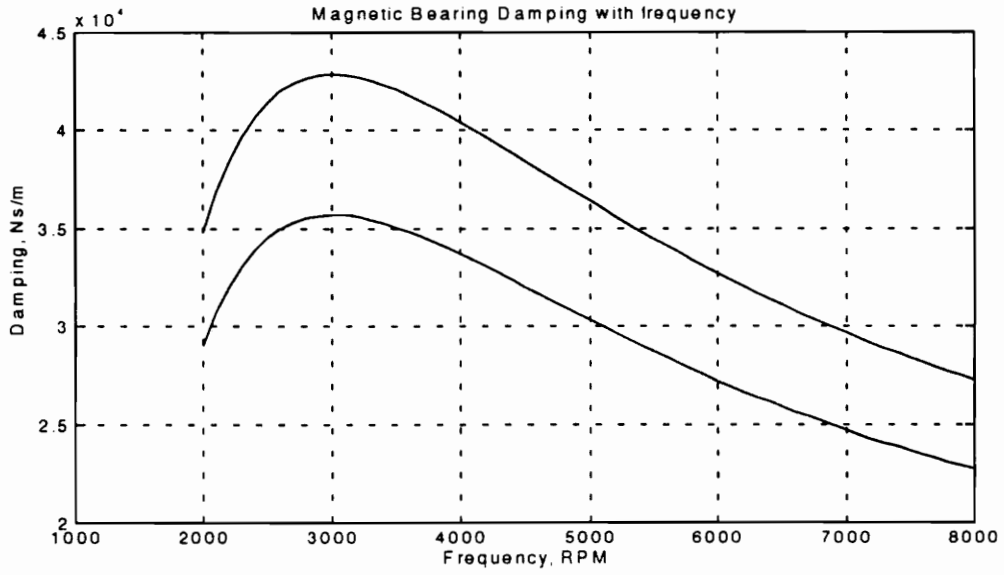

(b)

Figure 5.5a : Inboard (larger) and Outboard (smaller) Bearing Stiffness

Figure 5.5b: Inboard (larger) and Outboard (smaller) Bearing Damping

The results of the nominal forced response tests and the comparison to the experimental data is shown in Fig. 5.6a (outboard bearing response) and Fig. 5.6b (inboard bearing response). The dashed lines in the figures represent the experimental data, and the solid lines represent the simulations. It is evident from the figures that while the model does not perfectly predict the experimental results, many similarities do exist. The order of magnitudes of the results are very similar. The peak response level at the outboard bearing is around 0.46 mils for the experiments as compared to 0.51 mils for the simulations. At the inboard bearing, the peak response level for the experiments is around 0.11 mils as compared to 0.16 mils for the simulations. The critical speed for the outboard bearing occurs at around 5000 RPM for the simulations, and between 4000 and 5000 RPM for the experiments. At the inboard bearing, the critical speed occurs between 4000 and 5000 RPM for both the experiments and simulations. Finally, the general shapes of the responses for both bearings in simulation and experiment are similar, and at the outboard bearing, the responses match up almost identically for the range from 2000-4000 RPM. For all these reasons, we consider the model of the system to be valid in predicting the general behavior of the rotor/bearing system.

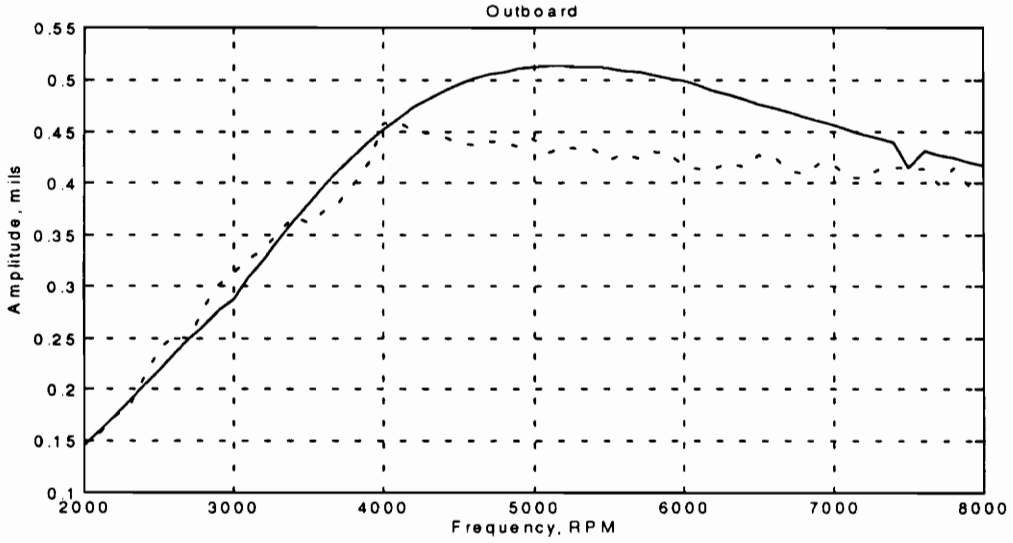

(a)

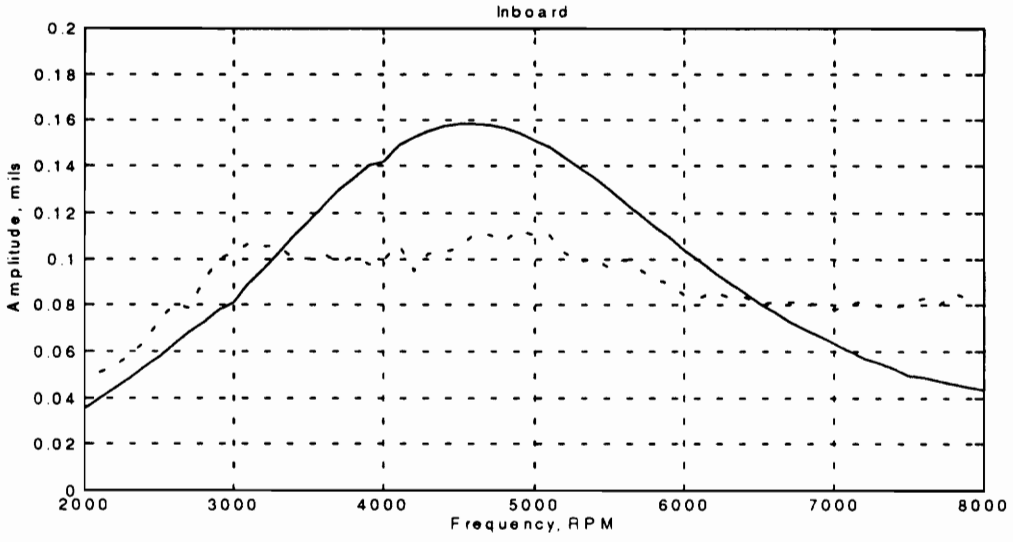

(b)

Figure 5.6a: Outboard Nominal Forced Response

Figure 5.6b: Inboard Nominal Forced Response

Both figures: (solid = theoretical, dashed = experimental)

5.3 Parameter Variation Experimentation

To understand the effects that controller parameters have on the rotor's response, two parameters were varied in the control system and the rotor's response was viewed at each variation. The first experiment varied the proportional gain, and the second varied the integral gain.

5.3.1 Variation of Proportional Gain

The two values of proportional gain at which we collected forced response data were Kp = 0.85, then Kp = 1.7. The integral gain was held constant at IG = 10. As with the nominal forced response case, the balance condition was acquired first, then the response with the known unbalance taken, and the net response calculated. To get an idea of how the change affects the bearing properties, Figs 5.7a and 5.7b show the change in stiffness and damping at the outboard bearing as the proportional gain is doubled. Since the proportional gain affects only the gain, but not the phase of the control system, the real and imaginary parts of the transfer function will both double, resulting in the doubling of the stiffness *and* the damping.

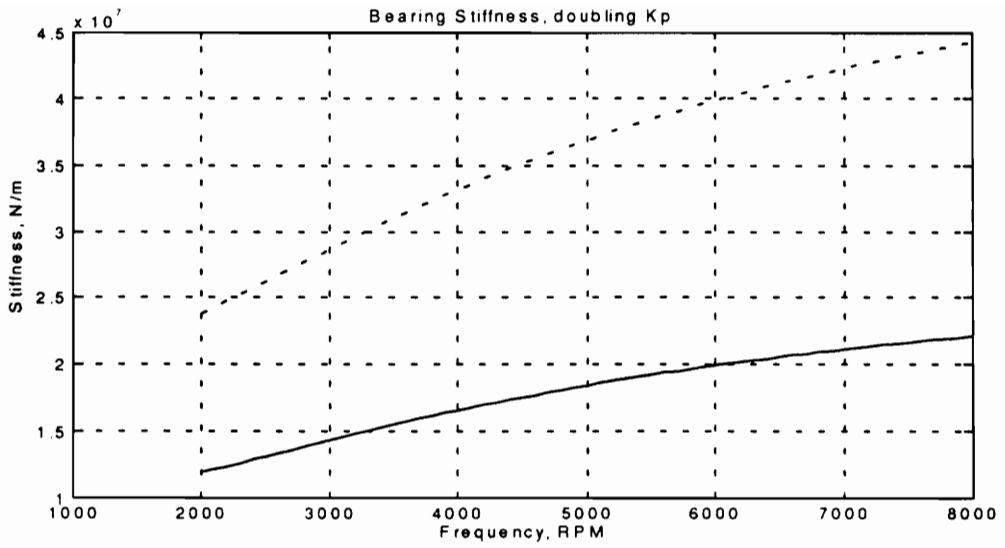

(a)

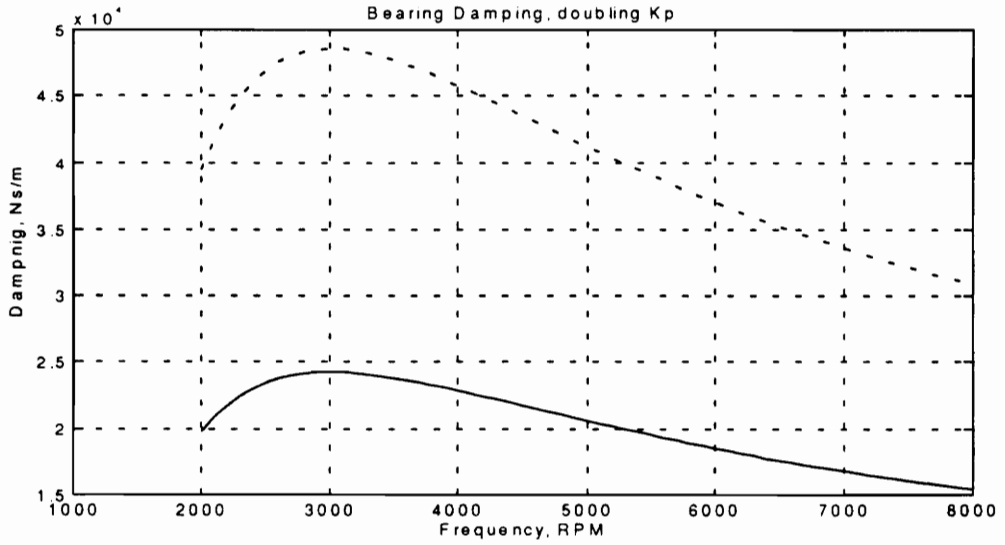

(b)

Figure 5.7a : Outboard Bearing Stiffness, Doubling Kp

Figure 5.7b: Outboard Bearing Damping, doubling Kp

Both figures: (solid=Kp=0.85, dashed=Kp=1.7)

5.3.1.1 Experimental Results

The experimental results show that increasing the proportional gain of the control system, which increases the stiffness and the damping, increases the rotor's first critical speed. This result is clearly shown in the plots of zero to peak amplitude response from 2000 RPM to 8000 RPM as the proportional gain is doubled as described in the previous section. Figures 5.8a and 5.8b show the results for the outboard and inboard bearing respectively. In Fig. 5.8a, the critical speed for the outboard bearing increases from around 3000 to around 5000 RPM as the proportional gain is changed. The peak amplitude level also increases as the critical speed increases. This is probably due to the larger amplitudes of unbalance force input at the higher critical speed. In Fig. 5.8b, the critical speed for the inboard bearing increases from around 2700 RPM to around 5000 RPM, and as with the outboard bearing, the peak amplitude level increases. Note also the lower amplitudes of response at the inboard bearing, because the unbalance was placed in the outboard disk of the rotor.

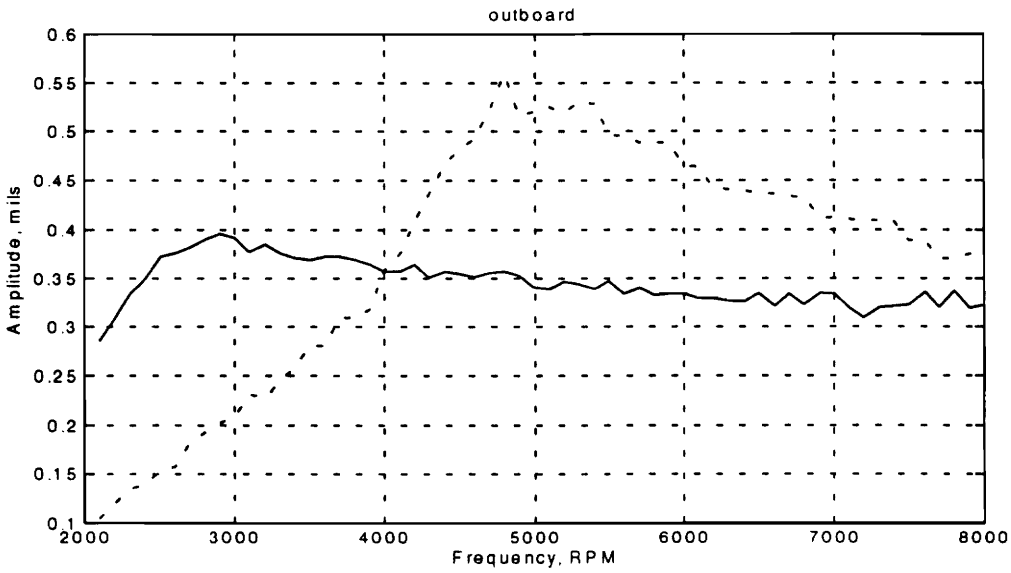

(a)

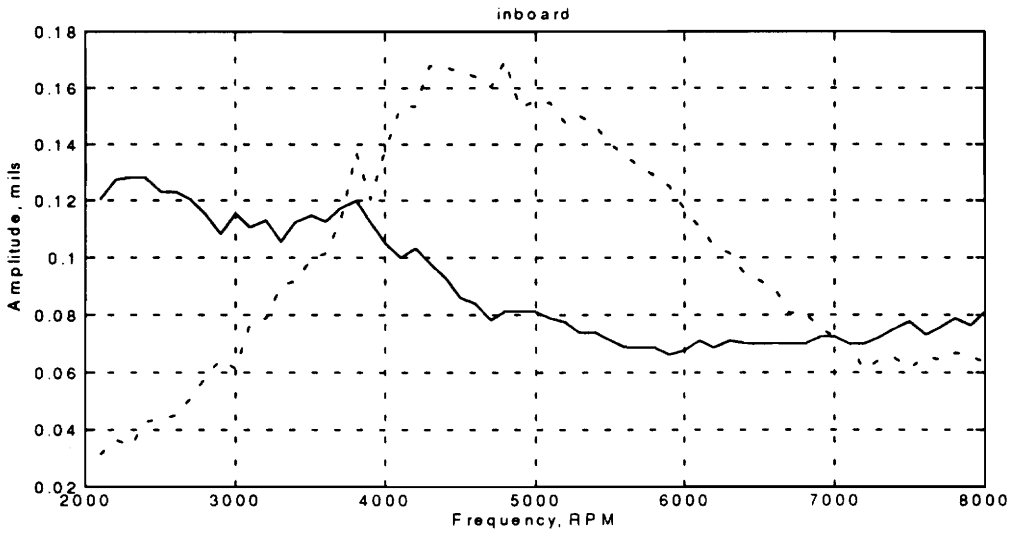

(b)

Figure 5.8a : Outboard Bearing Responses with doubling of K_p

Figure 5.8b: Inboard Bearing Response with doubling of Kp

Both figures: (solid=Kp=0.85, dashed=Kp=1.7)

5.3.1.2 Simulation Results

The simulations were performed to give a check on the experimental predictions of the effects of changing the parameters of the control system. It is evident from the experimental results of section 5.3.1.1 that increasing the proportional gain will increase the location of the first critical speed. Using the simulation technique from the previous chapter, we obtained the results shown in Figs 5.9a and 5.9b for the outboard and inboard bearings respectively. The solid line in each figure is the response with Kp=0.85, and the dashed line is the response with Kp=1.7

The results of the simulation for the change in proportional gain are very similar to those seen from the experimentation. At the outboard bearing, the peak amplitude response location (critical speed) increases from an area around 4000 RPM to around 6000 RPM, while maintaining the same level. At the inboard bearing, the critical speed increases from about 3000 RPM to about 5000 RPM, and the amplitude stayed relatively constant.

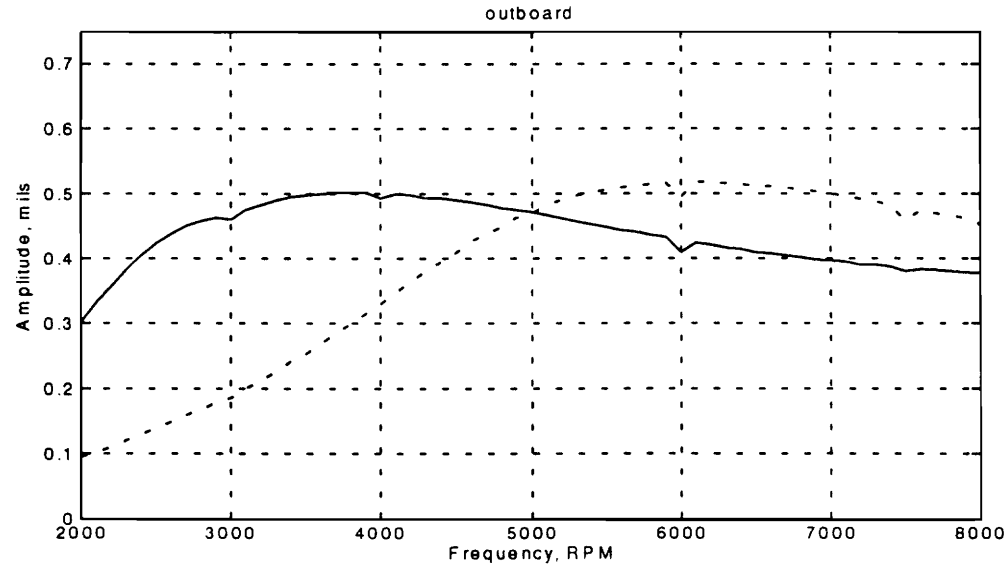

(a)

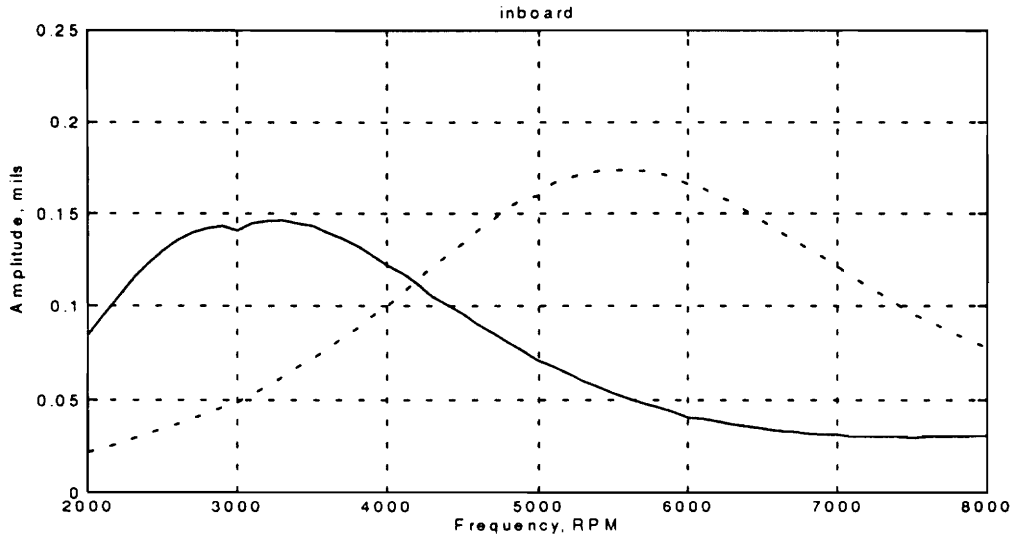

(b)

Figure 5.9a : Simulation Results for Doubling of Proportional Gain (Outboard)

Figure 5.9b: Simulation Results for Doubling of Proportional Gain (Inboard)

Both figures: (solid:Kp=0.85, dashed:Kp=1.7)

5.3.1.3 Experimental/Simulation Comparison

Tables 5.1 and 5.2 below summarize the results at the outboard and inboard bearings from the experiments and simulations with the proportional controller gain being doubled from 0.85 to 1.7.

Table 5.1: Outboard Bearing Critical Speeds and Amplitudes: Experimental and Simulations for Changing Kp

Case	Critical Speed (Simulation)	Critical Speed (Experimental)	Peak Amplitude (Simulations)	Peak Amplitude (Experimental)
K_p=0.85	3800 RPM	3000 RPM	0.5 mils	0.4 mils
K_p=1.7	6000 RPM	5000 RPM	0.52 mils	0.55 mils

Table 5.2: Inboard Bearing Critical Speeds and Amplitudes: Experimental and Simulations for Changing Kp

Case	Critical Speed (Simulation)	Critical Speed (Experimental)	Peak Amplitude (Simulations)	Peak Amplitude (Experimental)
K_p=0.85	3300 RPM	3000 RPM	0.15 mils	0.12 mils
K_p=1.7	5500 RPM	4800 RPM	0.17 mils	0.17 mils

As can be seen from the tabular results presented in Tables 5.1 and 5.2, the experiments and simulations do not exhibit perfect agreement on critical speeds and peak amplitudes. However, the trends in both are the same: as the proportional gain increased, the critical speed increases. The amount of increase in the critical speed in both the simulations and experiments was approximately the same (~2000 RPM). Also, the amplitude levels at each critical speed are similar for the experiments and the simulations.

5.3.2 Variation of Integral Gain

The two values of integral gain at which we collected forced response data were IG = 10, then IG = 5. The proportional gain was held constant at Kp = 0.85. As with the nominal forced response case, the balance condition was acquired first, then the response with the known unbalance taken, and the net response calculated. To get an idea of how the change affects the bearing properties, Figs 5.10a and 5.10b show the change in stiffness and damping at the outboard bearing as the integral gain is halved. The solid line represents the cases with integral gain set to IG=10, and the dashed line represents the cases with IG = 5. Figure 5.10a shows that changing the integral gain in this fashion does not affect the stiffness at all. Figure 5.10b shows that the damping is affected significantly by the change in integral gain, especially at low frequencies.

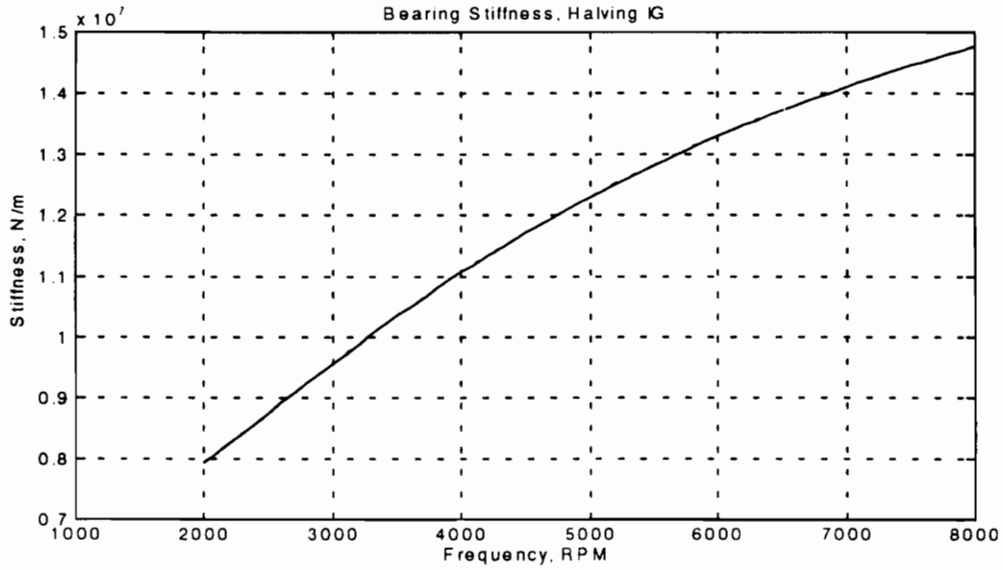

(a)

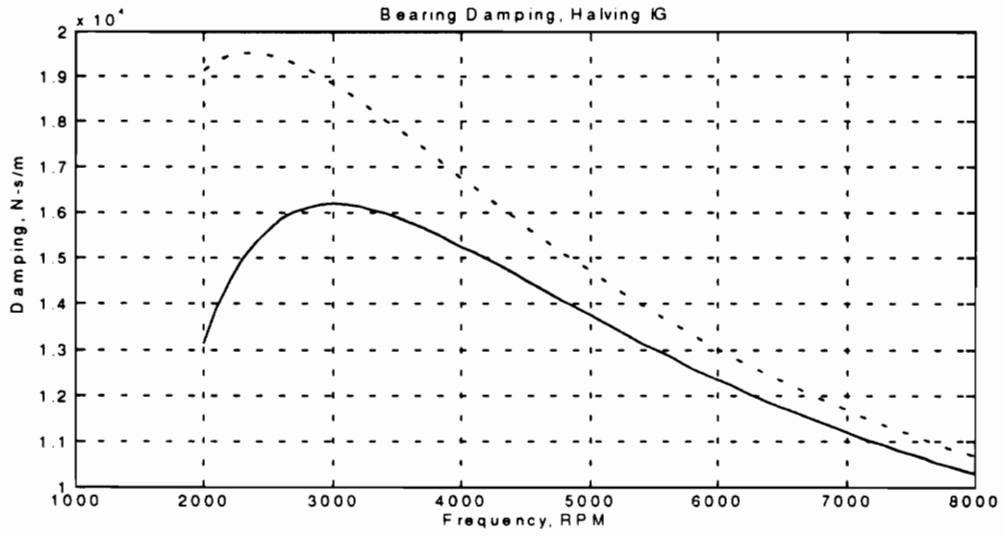

(b)

Figure 5.10a: Outboard Bearing Stiffness, Halving IG

Figure 5.10b : Outboard Bearing Damping, Halving IG

Both figures: (dashed:IG=5, solid:IG=10)

5.3.2.1 Experimental Results

The experimental results show that changing the integral gain has the effect of moving the peak response speed of the rotor. The amplitude of peak response is also affected, though not significantly. As seen in Fig. 5.11a, the zero to peak amplitude response at the outboard bearing, the peak amplitude response speed increases from about 2600 RPM with the integral gain set to IG =10, to about 3300 RPM with the integral gain set to IG = 5. The peak response speed is affected by the damping of the critical speed mode, and as the integral gain changes, the damping changes. This affects the location of the peak response, while the level of response is not significantly changed. The peak response level stays relatively the same, around 0.45 mils zero to peak. Figure 5.11b, the zero to peak amplitude response at the inboard bearing, shows a similar result. The peak amplitude response speed moves from around 3000 RPM with IG = 5 to around 3700 RPM with the IG = 10. Again, the peak response speed moves because of the change in the damping of the critical mode. The peak amplitude response level remains around 0.12 mils zero to peak for both cases at the inboard bearing.

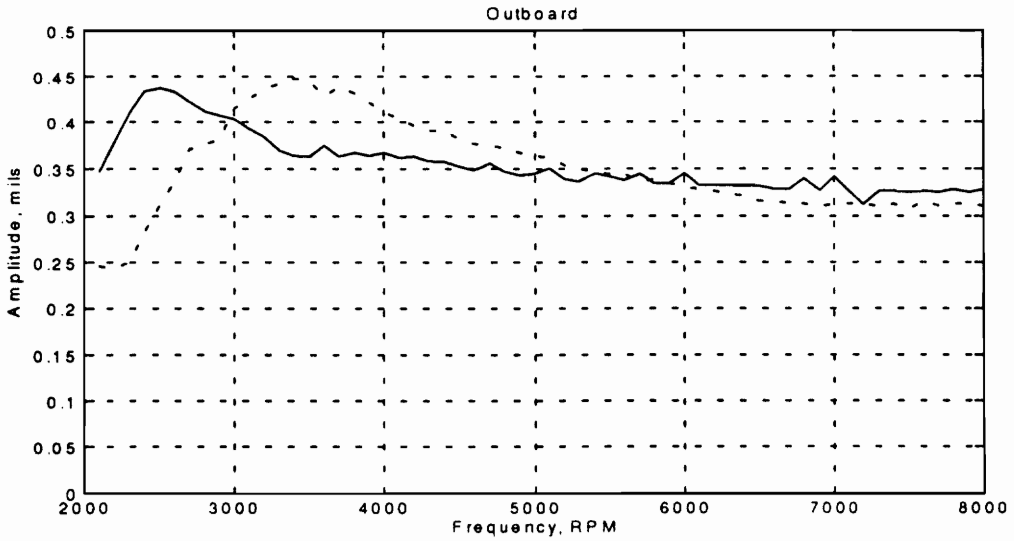

(a)

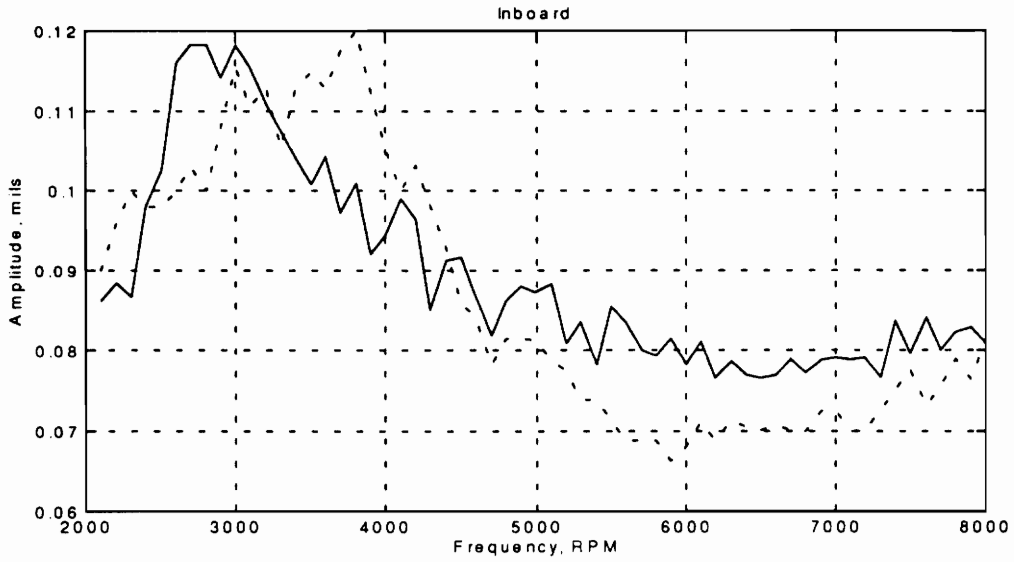

(b)

Figure 5.11a: Outboard Bearing Response for Halving IG

Figure 5.11b: Inboard Bearing Response for Halving IG

Both figures: (solid:IG=10,dashed:IG=5)

5.3.2.2 Simulation Results

The experimental results from the previous section have shown that changing the integral gain, which changes the damping of the bearings, moves the peak response speed and has a small affect on the peak response amplitude. Simulations performed using the methods described in chapter 4 resulted in the data shown in Fig. 5.12a and 5.12b, the zero to peak amplitude responses for the outboard and inboard bearing as the integral gain is changed.

Figure 5.12a, the outboard response as the integral gain is changed, shows that as the integral gain is changed from IG = 5 (the dashed plot) to IG = 10 (the solid plot), the peak amplitude location moves from around 3800 RPM to around 4300 RPM, while the zero to peak amplitude changes slightly, from 0.5 mils to 0.47 mils. In Figure 5.12b, the inboard response as the integral gain is changed, a similar trend occurs. As the integral gain is changed from IG = 5 (dashed plot) to IG = 10 (solid plot), the peak response speed changes from around 3000 RPM to around 3500 RPM. The peak amplitude changes slightly again, from 0.14 mils to 0.12 mils

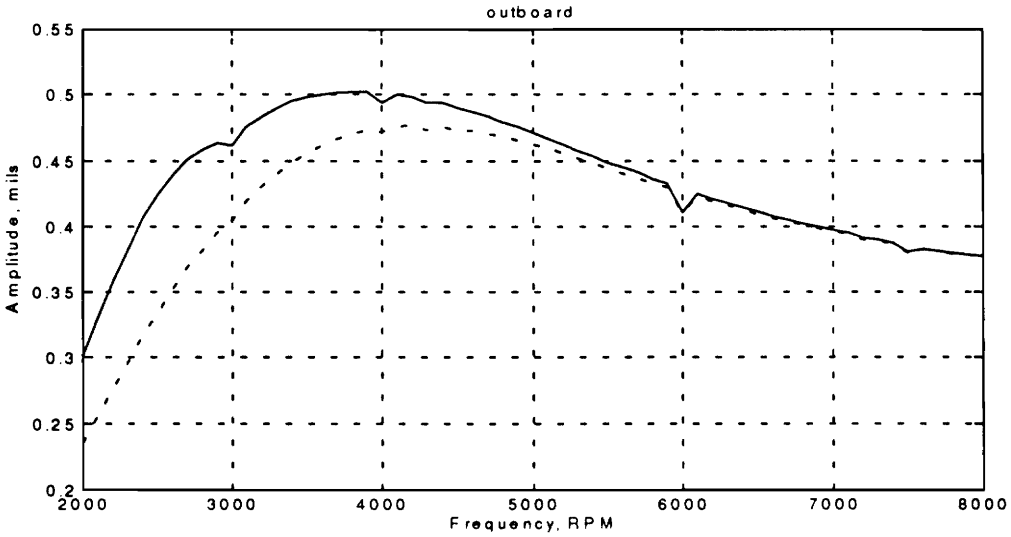

(a)

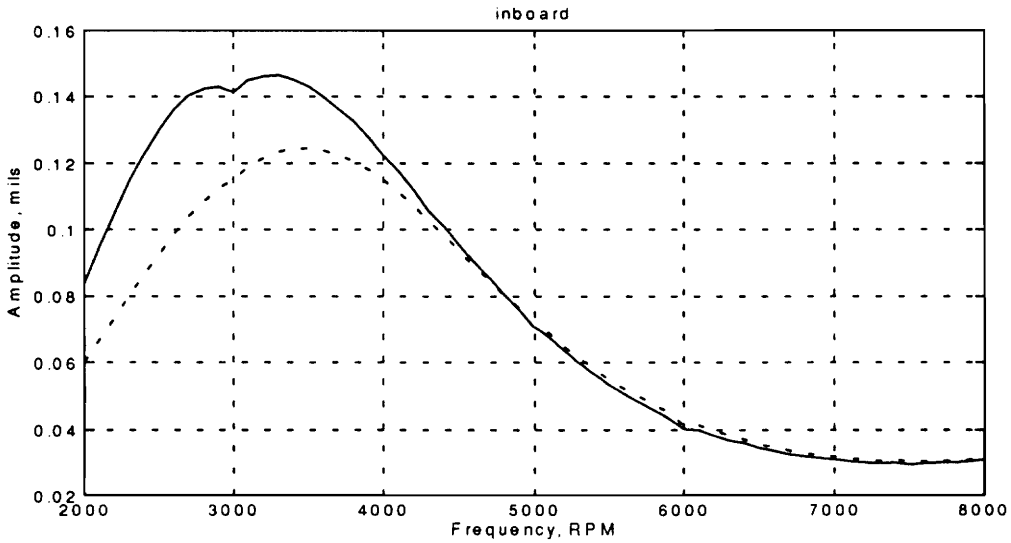

(b)

Figure 5.12a : Outboard Simulation Results for Halving IG

Figure 5.12b: Inboard Simulation Results for Halving IG

Both figures: (solid:IG=10,dashed:IG=5)

5.3.2.3 Experimental/Simulation Comparison

Tables 5.3 and 5.4 below summarize the results at the outboard and inboard bearings from the experiments and simulations with the integral controller gain being changed from IG = 5 to IG = 10.

Table 5.3: Outboard Bearing Critical Speeds and Amplitudes: Experimental and Simulations for Changing IG

Case	Critical Speed (Simulation)	Critical Speed (Experimental)	Peak Amplitude (Simulations)	Peak Amplitude (Experimental)
IG=5	4100 RPM	3300 RPM	0.47 mils	0.45 mils
IG=10	3800 RPM	2600 RPM	0.50 mils	0.45 mils

Table 5.4: Inboard Bearing Critical Speeds and Amplitudes: Experimental and Simulations for Changing IG

Case	Critical Speed (Simulation)	Critical Speed (Experimental)	Peak Amplitude (Simulations)	Peak Amplitude (Experimental)
IG=5	3500 RPM	3700 RPM	0.12 mils	0.12 mils
IG=10	3000 RPM	3000 RPM	0.14 mils	0.12 mils

As seen from Tables 5.3 and 5.4, the results from experiments and simulations do not agree perfectly. However, as with the change in proportional gain, the trends exhibited are the same.

Looking at Figs 5.11a and 5.12a, the experimental and simulation outboard bearing responses, the change in peak response speed from IG=10 to IG=5 is 300 RPM in the simulation and 700 RPM in the experiments. This shows that the change in the integral has the same effect in the experiments as predicted by the simulation, although the amount of change is different. The simulations predict well the experimental peak response amplitudes at each case of integral gain. Finally, we saw in Fig. 5.10b that the change in integral gain affected the damping primarily at low frequencies, and at high frequencies, the damping was essentially the same for each gain. The simulation in Fig. 5.12a, which shows the responses coming together at around 5000 RPM, gives the expected result. It also predicts the behavior experimentally, in Fig. 5.11a. As in the simulations, the responses come together around 5000 RPM, when the damping ceases to be significantly different for each case of integral gain.

Looking at Figs. 5.11b and 5.12b, the experimental and simulation inboard responses of the rotor with a change from IG=10 to IG=5 in the integral gain, the similarities are apparent. The simulations show that as the integral gain is halved, the peak response speed increases by about 500 RPM. This predicts well the change in experimental peak response speed of 700 RPM. Also, as with the outboard bearing, the response levels given by the simulation predict well the experimental levels. The peak

amplitudes are similar for each case of gain in the simulations and experiments, and the responses come together at around 4500 RPM once the difference in damping from the change in the gain is insignificant.

5.4 Chapter Summary

This chapter has presented the results of the experiments and simulations performed to determine the effects of changing proportional and integral gains in the control system. By comparing the simulations and experiments, we also gained an understanding of the predictive ability of the model of the rotor/bearing system. We saw that changing the afore mentioned gains produced the same effects in the simulations and the experiments. In particular, changing the proportional gain changed the rotor's critical speed significantly, while leaving the peak amplitude unchanged. Changing the integral gain moved the rotor's peak response speed a small amount, and left the peak amplitude basically unchanged.

Comparing the results obtained in this research to the previous work, the similarities are apparent. Williams, Keith, and Allaire [16] reported that variation of the integral gain affects the bearing damping mainly at low frequencies, as reported here. In their experimental work, they saw a slight increase in the rotor's peak response speed as the integral gain decreased. They also reported a significant change in the amplitude of peak response as the integral gain decreased. The first experimental result is corroborated in this work. The second result is not because the gain levels and amount of change in

gain made in their work were significantly higher than in this work, resulting in a larger change in damping and a larger change in amplitude. Keith et al [9] reported that an increase in proportional gain increases the bearing stiffess, thereby increasing the first critical speed of the rotor. This result matches the results obtained in this work. As a last comparison, Allaire, Humphris, and Barrett [1] show again that increasing proportional gain results in an increase in the first critical speed.

In the following chapter, we provide several conclusions from this work, and make several recommendations for further research in this area.

Chapter 6: Conclusions and Recommendations

6.1 Conclusions

From the research performed in the this thesis, we can make several conclusions concerning the modelling of this rotor/bearing system, and the effects of changing the gains of the control system on the performance of the rotor. These conclusions are:

- The model of the rotor/bearing system is an adequate model for predicting the behavior of the magnetic bearing supported rotor under unbalance loading.
- The increase of proportional gain in the control system produces an increase in the rotor's first critical speed by increasing the bearing stiffness across the range of frequencies.
- The increase of integral gain in the control system produces a small decrease in the peak response speed of the rotor at lower speeds, while leaving the rotor amplitudes insignificantly changed at higher speeds. This is due to the low frequency region in which this change affects the bearing damping.

The following section explains these conclusions and offers several explanations and suggestions.

6.1.1 Rotor/Bearing System Model

The finite element model of the rotor itself, being derived from elastic properties and known rotor dimensions, was fairly fault free. However, to fully model the

characteristics of the bearings, we must possess a detailed, rigorous model of the control system. Only this way will the behavior of the rotor under the influence of the magnetic bearings be fully predictable through simulations. As seen in the comparisons between experiments and simulations in the previous chapter, the behavior was not fully predictable. This leads to the conclusion that the bearing properties used in the simulations were not indicative of the true nature of the bearings. We did demonstrate the verification of the control system transfer function experimentally, so the model of some other portion of the control loop must be at fault. A possible explanation is that some of the portions of the loop which were modelled as DC gains may in fact possess some frequency dependent behavior which was not modelled. This would change the frequency response of the overall control loop and thus change the bearing properties. It is also possible that the mass unbalance used to excite the rotor excited harmonics of the running speed frequency. This would mean that the unbalance force was distributed across several frequencies, and the one-times synchronous response did not receive the full unbalance force, as the simulations assumed.

Overall, the model used for the rotor/bearing system, though not fully predictive of the behavior of the rotor, performed adequately for our purposes. Particularly, the model predicted well the trends exhibited in the rotor as a result of changing the control system gains.

6.1.2 Changing Proportional Gain

The changing of the proportional gain in the control system had the primary effect of moving the first critical speed of the rotor. The proportional gain affects the real part of the control system frequency response, which in turn directly affects the stiffness of the bearings with frequency. In a simple dynamic system, when the stiffness is increased, the natural frequency increases. Similarly, with a magnetic bearing supported rotor, when the bearing stiffness is increased, the critical speed goes up as well. This was observed at both the inboard and outboard bearings. The amount of increase of the critical speed as it relates to amount of increase of proportional gain was not studied. However, the experiments and simulations performed provide a solid conclusion on the effects of the proportional gain.

6.1.3 Changing Integral Gain

The changing of the integral gain shifted the peak response speed of the rotor by changing the damping of the bearings while leaving the bearing stiffness unchanged. The effects of this gain change were only observed at low frequencies (<5000 RPM) since the properties (stiffness and damping) were identical above this value for both cases of integral gain. Even with the change in damping from the change in integral gain at low frequencies, the effects on the response were not very significant. We expect a change in damping to result in a change in peak response amplitude, but both the experimental and simulation results showed small change in this value. This is probably due to the fact that the damping is very low in the first place. The shifting in peak response speed that was

observed with the change in damping from integral gain is something that we expected to see. However, the shifting in peak response speed can be accomplished just as easily with a change in proportional gain, while maintaining the same damping at the critical mode.

6.2 Recommendations

We have shown and concluded that changing the proportional gain has a large effect on the response of the magnetic bearing supported rotor. We have also concluded that changing the integral gain, while exhibiting small effects, does not significantly change the response of the rotor. In this section, we make several recommendations for magnetic bearing control system design in the future, as well as recommendations for this study. Our recommendations are:

- Identify without uncertainty the frequency dependent behavior of all the components in the control system.
- Implement derivative control in a future control system.
- Model the flexible coupling between the motor and the shaft.
- Obtain more quantatative results of the effects of changing control system parameters.
- Advanced Control Methods

.

6.2.1 Control System Identification

The control loop in a magnetic bearing system is made up of many components which contribute in their own way to the overall control system. It is imperative that the characteristics of these components be known fully and in detail before making any large changes in the control system. This way, the characteristics of the entire control loop are known in much better detail and the response of the rotor to changes in the control system is better predicted. This is especially important in the design stage when the behavior of the rotor with the magnetic bearings is uncertain.

6.2.2 Derivative Control

From the conclusions in the previous section, we can recommend that proportional control is a useful tool in the control of unbalance response of magnetic bearing supported rotors. Integral control is necessary to remove steady state error from the magnetic bearing supported rotor, but it is not recommended as a method of shaping the unbalance response of the rotor. Another option which would improve the magnetic bearing system is to implement derivative control in the control loop. Derivative control affects the damping of the bearings without affecting the stiffness. As seen in chapter 3, the increase in damping with an increase in the derivative gain is uniform across the range of frequencies considered. Also, the amount of increase of damping is quantified much easier with an increase in derivative gain than with an increase in integral gain. This makes the effects of an increase in derivative gain easier to predict and understand.

6.2.3 Rotor Model Expansion

An expansion of the model of the rotor to include the true properties of the flexible coupling between the rotor and the motor would result in the system's characteristics being represented more accurately. The hanging half-weight model used for the coupling in this study, while representative of the weight of the coupling, does not represent at all the length and diameter of the coupling. Including the coupling's dimensions and shape in the model would improve the model's accuracy in a comparison to experimental results and aid in control system design by giving more confidence in the model.

6.2.4 Quantatative Results and Advanced Control Methods

Another way to improve this study would be to perform more experiments to obtain quantitative measures of the effects of changing control system parameters. This way, we would present more numerical conclusions on the effects of these changes. These numeric results would be useful not only for this test rig and this study, but also as a reference for future work in this area.

As a last recommendation, we bring up the possibility of more advanced control methods applied to magnetic bearing control systems. Several control methods other than

P-I-D control were mentioned in the literature, and are options for future work, including the work by Chen and Darlow, and Salm. The choice of control method often depends on the speed range and variation of the machine. If the machine is to be run at a constant speed with little variation, then the unbalance response at this one running speed frequency can be attenuated using notch filtering, as suggested by Knospe and Humphris. If speed is to be varied, then a control method which stabilizes the rotor across the range of speeds is a more viable solution. Another idea is to use an Linear-Quadratic-Regulator control law, which minimizes a performance index with respect to the control input and the state variables. Since it is impossible to measure all the rotor states, an observer would have to be built. This type of control scheme, while not addressing the rotor response directly, would produce a control law which stabilizes the rotor while keeping control forces low.

Appendix A.1: Derivation of Current and Position Stiffnesses

From Humphris et al [1], we see that the force that the magnetic bearing exerts on the journal is a function of both the current in the bearing and the size of the air gap between the bearing and the journal, as in equation (A.1). This is a nonlinear relationship and must be linearized to perform the analysis for this research;

$$F = \mu_o A N^2 \frac{i^2}{x^2} \tag{A.1}$$

where:

i = current in the bearing

x = air gap between bearing and journal

μ_o = permeability of free space

A = projected bearing area

N = number of coil turns per magnetic pole

To linearize this expression, we use a Taylor series expansion about the equilibrium point, which in this case corresponds to the bias current in the bearing and the nominal air gap between the bearing and the journal. The Taylor series expansion for the force expression takes the following form:

$$F = \frac{\partial F}{\partial i}\Big|_o i + \frac{\partial F}{\partial x}\Big|_o x \tag{A.2}$$

where the partial derivatives are evaluated at the operating point, which we will call i_o and x_o. Taking the partial derivatives gives us the expressions in equations (A.3) and (A.4):

$$\frac{\partial F}{\partial x} = \frac{-2\mu_o AN^2 i^2}{x^3} \tag{A.3}$$

$$\frac{\partial F}{\partial i} = \frac{2\mu_o AN^2 i}{x^2} \tag{A.4}$$

Substituting these into equation (A.2) and evaluating at the operating point gives:

$$F = \frac{2\mu_o AN^2 i_o}{x_o^2} i + -\frac{2\mu_o AN^2 i_o^2}{x_o^3} x \tag{A.5}$$

or

$$F = k_i i + k_x x \tag{A.6}$$

where:

$$k_i = \frac{2\mu_o AN^2 i_o}{x_o^2} \tag{A.7}$$

$$k_x = -\frac{2\mu_o AN^2 i_o^2}{x_o^3} \tag{A.8}$$

These are the relations stated in equations (2.19) and (3.13), respectively.

References

[1]. Allaire, P.E., Humphris, R.R., and Barrett, L.E., "Critical Speeds and Unbalance Response of a Flexible Rotor in Magnetic Bearings", Proceedings of the 1st European Sponsored Turbomachinery Symposium, pp. 111-120, 27-28 October, 1986

[2]. Barrett, L.E., "Modeling of Magnetic Bearings Supported Rotors," ROMAG '91, Magnetic Bearings and Dry Gas Seals, International Conference and Exhibition, 13-15 March, 1991

[3]. Chen, H.M. and Darlow, M.S., "Magnetic Bearing with Rotating Force Control", Journal of Tribology, Transactions of the ASME, Vol. 110, pp. 100-105, January 1988

[4]. Ehrich, Fredric F., Editor-In-Chief Handbook of Rotordynamics, McGray-Hill, New York, New York, 1992

[5]. Franklin, G.F., Powell, J.D., and Emami-Naeini, A., Feedback Control of Dynamic Systems, Addison -Wesley, Reading, MA, 1991.

[6]. Franklin, G.F., Powell, J.D., and Workman, M.L., Digital Control of Dynamic Systems, Second Edition, Addison-Wesley, Reading, MA, 1990

[7]. Hale, F.J., Introduction to Control System Analysis and Design, Second Edition pp. 193-216, Prentice Hall, Englewood Cliffs, NJ, 1988

[8]. Humphris, R.R., Kelm, R.D., Lewis, D.W., and Allaire, P.E., "Effect of Control Algorithms on Magnetic Journal Bearing Properties," Journal of Engineering for Gas Turbines and Power, Transactions of the ASME, Vol. 108, pp. 624-633, October 1986

[9]. Keith, F.J., Williams, R.D., Allaire, P.E. and Schafer, R.M., "Digital Control of Magnetic Bearings Supporting a Multimass Flexible Rotor," Tribology Transactions, Vol. 33, no. 3, pp. 307-314, 1990

[10]. Maslen, E.H., and Bielk, J.R., "A Stability Model for Flexible Rotors with Magnetic Bearings," Journal of Dynamic Systems, Measurement, and Control, Transactions of the ASME, Vol. 114, pp. 172-175, March 1992

[11]. Maslen, E.H., Hermann, P., Scott, M., and Humphris, R.R., "Practical Limits to the Performance of Magnetic Bearings: Peak Force, Slew Rate, and Displacement Sensitivity," Journal of Tribology, Transactions of the ASME, Vol. 111, pp. 331-336, April 1989

[12]. Okada, Y., "Disturbance Observer Based Controller for Flexible Rotor Supported by Magnetic Bearings," Fourth International Symposium on Magnetic Bearings, International Center for Magnetic Bearings, Zurich, Switzerland, pp.53-58, August 1994

[13]. Ramesh, Krishnaswamy, "Advanced Analysis of Rotor/Bearing Systems for Stability and Response", Ph.D. Dissertation, Department of Mechanical Engineering, Virginia Polytechnic Institute and State University, April 1996

[14]. Salm, J.R. "Active Electromagnetic Suspension of an Elastic Rotor: Modelling, Control, and Experimental Results," Journal of Vibration, Acoustics, Stress, and Reliability in Design, Transactions of the ASME, Vol. 110, pp. 493-499, October 1988.

[15]. Schweitzer, G., Bleuler, H., and Traxler, A., *Active Magnetic Bearings: Basics, Properties, and Applications of Active Magnetic Bearings*, 1st edition, VDF, Zurich, Switzerland, 1994

[16]. Williams, R.D., Keith, F.J., and Allaire, P.E., "Digital Control of Active Magnetic Bearings," IEEE Transactions on Industrial Electronics, Vol. 37, No.1, pp.19-27, February 1990

[17]. Youcef-Toumi, K., and Reddy, S., "Dynamic Analysis and Control of High Speed and High Precision Active Magnetic Bearings," Journal of Dynamic Systems, Measurement, and Control, Transactions of the ASME, Vol. 114, pp. 623-633, December 1992

Vita

David R. Schmiel was born on September 16, 1972 in Altoona, Pennsylvania, when his father was teaching history at St. Francis College in Loreto, PA. This idyllic existence was soon changed when David's father joined the U.S. Department of State in 1973. The next fourteen years from 1974-1988 saw David and his family spend more than half of these years in such exotic locales as Stockholm, Sweden, Durban, South Africa, Mombasa, Kenya, and the non-exotic locale of Djibouti, Djibouti. Returning to the United States for good in 1988, David enrolled in the rigourous college preparatory cirriculum at Thomas Jefferson High School for Science and Technology in Alexandria, VA. After graduating from Jeffferson in June of 1990, David enrolled in Virginia Tech as a naive General Engineering freshman in August of the same year. Though overwhelmed at first, he soon learned the tricks of the trade (i.e. all the stuff you learn in EF is useful, you really do have to study in college, and the Balcony has dime beers on Friday afternoons) and managed to graduate Magna Cum Laude with a Bachelor of Science in Mechanical Engineering in May of 1994. In his senior year, David suffered a temporary loss of sanity and enrolled for two graduate level courses to get ahead in the Masters' program at Virginia Tech. Entering this program in the fall of 1994, he finished his coursework quickly and his research not so quickly. Now, in the spring of 1996, he is defending his thesis and looking forward to continuing his career with PDI (Propulsion Dynamics Inc.) in Annapolis, MD as a Controls Engineer. Right now, the letters Ph.D. scare David half to death.

David Schmiel